SUPPLEMENT TO "RAPID ASSEMBLY AND CRYSTALLIZATION OF A FOSSIL, LARGE-VOLUME, SILICIC MAGMA CHAMBER"

Michael P. Eddy, Samuel A. Bowring, Robert B. Miller, Jeffrey H. Tepper

Lithologic Descriptions

Peralkaline granite: Misch (1965) first recognized peralkaline granite within the Golden Horn batholith (GHB) and the rock was subsequently described by Stull (1969). It forms a ~400 m thick sheet of leucocratic, medium-grained granite dominantly composed of perthite, quartz, and sodic amphiboles (riebeckite, arfvedsonite) exposed in a down-dropped fault block (72 km^2) in the southeastern portion of the batholith (Fig. 1B and 1C). The presence of dark blue sodic amphibole is diagnostic in the field. Quartz occurs as large (5-10 mm) rounded crystals and in granophyric intergrowths between large grains (Stull, 1969). Miarolitic cavities are abundant within this lithology and range from several millimeters to one meter in diameter. The cavities are filled with diverse minerals, including several unique to the GHB (Boggs, 1984). Dikes of the hypersolvus granite cut the peralkaline granite and establish a relative age relationship between the two lithologies. The normative mineralogy of the peralkaline granite plots near the 0.2 GPa H_2O-saturated eutectic in the Ab-Or-Qz system (Fig. DR1).

Hypersolvus granite: Hypersolvus granite was first mapped and described by Stull (1969). It forms two subhorizontal sheets exposed in the southeastern portion of the GHB (Fig. 1B and 1C). The first sheet is only exposed at very high elevations and remains poorly documented and undated. The second sheet is ~750 m thick and is exposed underneath the peralkaline granite. The contact between the two lithologies is sharp and marked by highly weathered hypersolvus granite (Stull, 1969), and the sheet's lower contact with the rapakivi granite appears to be gradational. The hypersolvus granite is primarily composed of perthite, quartz, biotite, and hornblende and is distinguished from the peralkaline granite based on the absence of sodic amphiboles and the presence of biotite. Miarolitic cavities are abundant. The normative mineralogy of the hypersolvus granite plots just below the 0.2 GPa H_2O-saturated eutectic in the Ab-Or-Qz system (Fig. DR1). The current areal exposure of this unit is largely restricted to the down-dropped fault block (72 km^2) in the SE of the GHB. However, a thin screen of hypersolvus granite that extends along the west side of the batholith suggests that it may have once covered a larger area. Nevertheless, we use the 72 km^2 area of the fault block to calculate a minimum volume estimate for the unit and neglect the undated upper hypersolvus sheet in our calculations.

Rapakivi granite: The rapakivi granite was described in detail by Stull (1969, 1978). It is coarse grained and dominantly composed of plagioclase, orthoclase, quartz, and biotite ± hornblende. Perthitic orthoclase mantled with plagioclase (rapakivi texture) is pervasive and is a distinguishing characteristic in the field. Enclaves are common within the rapakivi granite and range from small (<1 cm) clots of mafic minerals to meter-scale, fine-grained enclaves. Mapping shows that the rapakivi granite forms a sheet-like body that extends across most of the batholith (303 km^2) with a minimum thickness of ~1400 m (Fig. 1B and

1C). Smaller, tabular bodies of leucogranite are common at high elevations within the rapakivi granite and may represent segregations of high-SiO_2 melt (Bachmann and Bergantz, 2004; Lee and Morton, 2015) or intrusion of a different melt composition after the rapakivi granite had mostly crystallized. The normative mineralogy of the rapakivi granite plots along a linear array in the Ab-Or-Qz ternary (Fig. DR1). This array reflects systematic variations in the chemistry of the rapakivi granite that correlate with each sample's vertical position within the sheet. These variations may reflect the vertical stratification expected to develop as silicic magma chambers differentiate (e.g., Lee and Morton, 2015), suggesting that these whole rock analyses do not represent liquid compositions and precluding their use in depth estimates.

Heterogeneous granite: Heterogeneous granite is exposed in the NW part of the batholith (Fig. 1B and 1C) as a 650-m-thick sheet-like body. Internal contacts are present and range from sharp to gradational, implying that the unit is composed of many individual intrusions. However, we could not split the heterogeneous granite into smaller map units due to poor exposure. The rocks are dominantly leucocratic granites and include both perthite-bearing and two-feldspar varieties. A distinctive, ~100-m-thick, fine-grained biotite granite forms the uppermost part of the heterogeneous granites and is found directly underneath the rapakivi granite over a wide area. We project the heterogeneous granite under the granitoid portions of the batholith (303 km^2) for our volume estimate.

Granodiorite: Granodiorite is exposed at low elevations in the extreme NW of the batholith (Fig. 1B). This map unit is composed of heterogeneous granitoids with a higher color index than the heterogeneous granites. The dominant lithology is a medium-grained hornblende granodiorite that includes some rapakivi-textured feldspars.

Quartz Diorite: A small body of hornblende quartz diorite occurs along the SW boundary of the GHB (Fig. 1B). It is medium grained and includes angular xenoliths of the host rock along its outer margin.

Unnamed Subvolcanic Stock: A subvolcanic rhyolitic stock intrudes the rapakivi granite in the NW of the GHB (Fig. 1B). At lower elevations it is a fine-grained, quartz-rich granite and grades into porphyritic rhyolite at higher elevations. The rhyolite is vesiculated and contains quartz phenocrysts, pieces of pumice, and small angular lithic fragments. Its relationship to the GHB is unclear. However, it must postdate the rapakivi granite based on the intrusive contact between the two units.

Al-in-Hornblende Barometry

In order to better assess the emplacement depth of the GHB, we calculated pressures for two samples of the rapakivi granite (NC-MPE-086: 48.57338 -120.63071 and NC-MPE-503: 48.64422 -120.75922) using the Al-in-hornblende barometer. This barometer is based on a linear relationship between the intrusion depth of silicic liquids and the total aluminum content (Al_{tot}) in hornblende. However, the silicic liquid must have been saturated with plagioclase, potassium feldspar, biotite, hornblende, titanite, quartz, magnetite or ilmenite, and a fluid phase during final crystallization for accurate pressure determinations. The

required mineral assemblage was identified in thin section, and the presence of both magnetite and ilmenite was confirmed using energy dispersive spectrometry (Fig. DR2). Hornblende and plagioclase core and rim compositions were measured using a 5 μm spot size on the MIT JEOL-JXA8200 using a 15 kV accelerating voltage and 10 nA beam current. The results are reported in Tables DR1 and DR2. Pressures were calculated using pairs of plagioclase-hornblende cores and plagioclase-hornblende rims using the calibration of Anderson and Smith (1995). Temperatures were estimated using the Blundy and Holland (1990) plagioclase-hornblende thermometer. All temperature and pressure estimates are reported in Table DR3.

The calculated pressures range from 0.05 to 0.30 GPa with an associated uncertainty of 0.06 GPa. Three measurements of hornblende rims give pressures lower than the experimental calibration of the Al-in-hornblende barometer (0.25 GPa: Schmidt, 1992) and hornblende-plagioclase thermometry for these samples gives temperatures below the H_2O-saturated solidus for granitic melts at pressures of <0.5 GPa (Ebadi and Johannes, 1991). Therefore, these results likely do not provide accurate pressure estimates. The remaining measurements give magmatic temperatures and consistent pressures. A mean of these values gives 0.25 ± 0.06 GPa and is at the lower limit of the experimental calibration for the barometer.

Zircon Petrography

Fig. DR3 shows representative cathodeluminescence (CL) images of zircon from GHB granitoids. Imaging was done on the JEOL JXA-733 microprobe at the Massachusetts Institute of Technology using a beam current of 10 nA. Oscillatory zoning is common in the zircons and indicates an igneous origin. No resorbed cores were seen in any of the images, supporting our interpretation that the GHB granitoids were emplaced above zircon saturation temperature. However, petrographic observations demonstrate that zircon is included in, and therefore predated or co-crystallized with, the major rock-forming minerals of the granitoid phases of the GHB (Fig. DR4). We conclude that zircon became saturated shortly after emplacement in the upper crust and that the duration of zircon crystallization approximates the duration of magma crystallization.

U-Pb Zircon Geochronology Methods

Zircons were separated and dated via chemical abrasion-isotope dilution-thermal ionization mass spectrometry (CA-ID-TIMS) following methods slightly modified from Mattinson (2005) and outlined in Appendix A for Eddy et al. (2016). All of the isotopic measurements were made on the VG Sector 54 thermal ionization mass spectrometer (TIMS) at the Massachusetts Institute of Technology and are presented in Table DR4. Pb isotopes were measured by peak hopping on a Daly detector and corrected for fractionation based on repeat analyses of the NBS 981 Pb isotopic standard. U was measured statically on Faraday cups and corrected for fractionation using the known ratio of $^{233}U/^{235}U$ in the EARTHTIME ^{205}Pb-^{233}U-^{235}U isotopic tracer (Condon et al., 2015; McLean et al., 2015). We assume that zircon does not incorporate initial common Pb (Pb_c) during

crystallization and that all measured ^{204}Pb arises from laboratory contamination. We correct for this contamination following the procedures outlined in McLean et al. (2011), using a laboratory Pb_c isotopic composition of $^{206}Pb/^{204}Pb$ = 18.145833 ± 0.475155 (1σ abs.), $^{207}Pb/^{204}Pb$ = 15.303903 ± 0.295535 (1σ abs.), and $^{208}Pb/^{204}Pb$ = 37.107788 ± 0.875051 (1σ abs.), calculated from 149 procedural blanks measured in the MIT isotope geochemistry lab between 2009 and 2015. The mass of Pbc measured in all of these procedural blanks is comparable to the range of Pb_c measured in the analyses presented in this paper and provides strong support for the assumption that no Pb_c is incorporated in zircon during crystallization.

The ^{230}Th isotope is a long-lived ($t^{1/2}$ = 75,400 yr) daughter isotope of ^{238}U, and preferential exclusion of Th during zircon crystallization can lead to initial secular disequilibrium. A correction for the resulting deficiency in radiogenic ^{206}Pb is described by McLean (2011) and Ickert et al. (2015) and is dependent on the $[Th/U]_{zircon}$ and $[Th/U]_{melt}$. The $[Th/U]_{zircon}$ is routinely calculated from zircon measurements using radiogenic ^{208}Pb and assuming concordance between the ^{232}Th-^{208}Pb and U-Pb systems. However, the $[Th/U]_{melt}$ is more difficult to constrain. Two potential methods can be used to derive $[Th/U]_{melt}$, 1) assume a $[Th/U]_{melt}$ using whole rock geochemical measurements or an average value for the rock type being investigated, or 2) use partition coefficients ($f_{ThU}=D_{Th}/D_U$) to calculate $[Th/U]_{melt}$ using $[Th/U]_{zircon}$. We compare both methods in Table DR5. For the approach using constant $[Th/U]_{melt}$, we use $[Th/U]_{melt}=2.8 \pm 1$ (2σ). This value encompasses the range seen in most igneous rocks (Machlus et al., 2015), and is consistent with whole rock measurements from granites within the GHB (Tepper, unpublished data). For the constant partition coefficient approach we use f_{ThU} =0.138 (Stelten et al., 2015) for granitic rocks and f_{ThU} =0.33 (Rubatto and Hermann, 2007) for the marginal tonalite/diorite and apply an arbitrary uncertainty of 1(2σ) on the resulting $[Th/U]_{melt}$.

The difference between data corrected using the two methods is minor and does not affect our interpretations of magma emplacement rates. We prefer the use of a constant f_{ThU} because it seems more reasonable that different $[Th/U]_{zircon}$ within a sample is a result of of changing melt composition either due to local depletion of trace elements around crystallizing trace phases or through changes in bulk melt composition due to fractional crystallization. Nevertheless, trace element partitioning between zircon and melt remains poorly constrained. The value used for granites in this paper (f_{ThU} = 0.138) is an average for coexisting zircon and high-SiO_2 melt erupted from Yellowstone (Stelten et al., 2015). These measurements offer an advantage over other datasets that report partition coefficients for zircon and coexisting high-SiO_2 melt in that it uses trace element measurements from zircon surfaces whose ^{238}U-^{230}Th dates are consistent with crystallization immediately prior to or concurrent with eruption. Other studies either lack corresponding age data or inevitably use a $[Th/U]_{zircon}$ calculated from a mixture of interior and surface domains that may not be in equilibrium with the matrix glass. In Fig. DR5 we show that the Stelten et al. (2015) value reproduces the range of whole rock Th/U measurements for GHB granites for the typical range of $[Th/U]_{zircon}$ values from our dataset.

Data reduction was done using the U-Pb_Redux software package (Bowring et al., 2011) and used the decay constants for ^{235}U and ^{238}U presented in Jaffey et al. (1971). All isotopic ratios are presented in Table DR4 and shown as concordia plots in Fig. DR6.

Magma Emplacement Rates

Magma emplacement rates were estimated for the GHB using our volume estimates (with no assigned uncertainty) and durations (Δt) calculated using Monte Carlo simulations with 10^7 iterations. The simulations found the difference between randomly selected dates from normal distributions with a mean value and 2σ variability equal to the weighted mean dates and 2σ uncertainty of our oldest and youngest sample within each unit. In cases where the oldest and youngest samples substantially overlap within uncertainty, we used the absolute value of the calculated difference to prevent negative durations. The distribution of results is shown in Fig. 2B. Fig. DR7 compares these results with magma emplacement rates, recalculated using the same technique, from previously published geochronologic data from upper-crustal granitoid plutonic complexes (Table DR6). As noted in the text, the rapakivi granite represents the highest magma emplacement rates documented in a granitoid plutonic complex.

References

Anderson, J.L. and Smith, D.R., 1995, The effects of temperature and fo_2 on the Al-in-hornblende barometer: American Mineralogist, v. 80, p. 549-559, doi: 10.2138/am-1995-5-615.

Annen, C., 2009, From plutons to magma chambers: thermal constraints on the accumulation of eruptible silicic magma in the upper crust: Earth and Planetary Science Letters, v. 284, p. 409-416, doi: 10.1016/j.epsl.2009.05.006.

Bachmann, O., and Bergantz, G.W., 2004, On the origin of crystal-poor rhyolites: extracted from batholithic crystal mushes: Journal of Petrology, v. 45, p. 1565-1582, doi: 10.1093/petrology/egh019.

Blundy, J., and Cashman, K., 2001, Ascent-driven crystallization of dacite magmas at Mount St Helens, 1980-1986: Contributions to Mineralogy and Petrology, v. 140, p. 631-650, doi: 10.1007/s004100000219.

Blundy, J., and Holland, T.J.B., 1990, Calcic amphibole equilibria and a new amphibole-plagioclase geothermometer: Contributions to Mineralogy and Petrology, v. 104, p. 208-224, doi: 10.1007/BF00306444.

Bowring, J.F., McLean, N.M., and Bowring, S.A., 2011, Engineering cyber infrastructure for U-Pb geochronology: Tripoli and U-Pb_Redux: Geochemistry, Geophysics, and Geosystems, v. 12, doi: 10.1029/2010GC003479.

Boggs, R.C., 1984, Mineralogy and geochemistry of the Golden Horn batholith, northern Cascades, Washington [PhD Thesis]: Santa Barbara, University of California, 187 p.

Coleman, D.S., Gray, W., and Glazner, A.F., Rethinking the emplacement and evolution of zoned plutons: geochronologic evidence for incremental assembly of the Tuolumne Intrusive Suite, California: Geological Society of America Bulletin, v. 32, p. 433-436, doi: 10.1130/G20220.1.

Condon, D.J., Schoene, B., McLean, N.M., Bowring, S.A., and Parrish, R.R., 2015, Metrology and traceability of U-Pb isotopic dilution geochronology (EARTHTIME tracer calibration part I): Geochimica et Cosmochimica, v. 164, p 464-480, doi: 10.1016/j.gca.2015.05.026.

Davis, J.W., Coleman, D.S., Gracely, J.T., Gaschnig, R., and Stearns, M., 2012, Magma accumulation rates and thermal histories of plutons of the Sierra Nevada batholith, CA: Contributions to Mineralogy and Petrology, v., 163, p. 449-465, doi: 10.1007/s00410-011-0683-7.

Eddy, M.P., Bowring, S.A., Umhoefer, P.J., Miller, R.B., McLean, N.M., and Donaghy, E.E., 2016, High resolution temporal and stratigraphic record of Siletzia's accretion and triple junction migration from nonmarine sedimentary basins in central and western Washington: Geological Society of America Bulletin, doi: 10.1130/B31335.1.

Ebadi, A., and Johannes, W., 1991, Beginning of melting and composition of first melts in the system Qz-Ab-Or-H2O-CO2: Contributions to Mineralogy and Petrology, v. 106, p. 286-295, doi: 10.1007/BF00324558.

Frazer, R.E., Coleman, D.S., and Mills, R.D., 2014, Zircon U-Pb geochronology of the Mount Givens Granodiorite: Implications for the genesis of large volumes of eruptible magma: Journal of Geophysical Research Solid Earth, v. 119, p. 2907-2924, doi: 10.1002/2013JB010716.

Gelman, S.E., Gutierrez, F.J., and Bachmann, O., 2013, On the longevity of large upper crustal silicic magma reservoirs: Geology, v. 41, p. 759-762, doi: 10.1130/G34241.1.

Ickert, R.B., Mundil, R., Magee Jr., C.W., and Mulcahy, S.R., 2015, The U-Th-Pb systematics of zircon from the Bishop Tuff: A case study in challenges to high-precision Pb/U geochronology at the millennial scale: Geochimica et Cosmochimica Acta, v. 168, p. 88-110, doi: 10.1016/j.gca.2015.07.018.

Jaffey, A.H., Flynn, K.F., Glendenin, L.E., Bentley, W.C., Essling, A.M., 1971, Precision measurement of half-lives and specific activities of 235U and 38U: Physical Review C, v. 4, p. 1889-1906, doi: 10.1103/PhysRevC.4.1889.

John, B.E., and Blundy, J.D., 1993, Emplacement-related deformation of granitoid magmas, southern Adamello Massif, Italy: Geological Society of America Bulletin, v. 105, p. 1517-1541, doi: 10.1130/0016-7606(1993)105<1517:ERDOGM>2.3.CO;2.

Lee, C.A., and Morton, D.M., 2015, High silica granites: terminal porosity and crystal settling in shallow magma chambers: Earth and Planetary Science Letters, v. 409, p. 23-31, doi: 10.1016/j.epsl.2014.10.040.

Leuthold, J., Muntener, O., Baumgartner, L.P., Putlitz, B., Ovtcharova, M., and Schaltegger, U., 2012, Tim resolved construction of a bimodal laccolith (Torres del Paine, Patagonia): Earth and Planetary Science Letters, v. 325-326, p. 85-92, doi: 10.1016/j.epsl.2012.01.032.

Machlus, M.L., Ramezani, J., Bowring, S.A., Hemming, S.R., Tsukui, K., and Clyde, W.C., 2015, A strategy for cross-calibrating U-Pb chronology and astrochronology of sedimentary sequences: an example from the Green River Formation, Wyoming, USA: Earth and Planetary Sciences, v. 413, p. 70-78, doi:10.1016/j.epsl.2014.12.009.

Mattinson, J.M., 2005, Zircon U-Pb chemical abrasion ("CA-TIMS") method: Combined annealing and multi-step partial dissolution analysis for improved precision and accuracy of zircon ages: Chemical Geology, v. 220, p. 47-66, doi: 10.1016/j.chemgeo.2005.03.011.

Matzel, J.E.P., Bowring, S.A., and Miller, R.B., 2006, Time scales of pluton construction at differeing crustal levels: Examples from the Mount Stuart and Tenpeak intrusions, North Cascades, Washington: Geological Society of America Bulletin, v. 118, p. 1412-1430, doi: 10.1130/B25923.1.

McLean, N.M., Bowring, J.F., and Bowring, S.A., 2011, An algorithm for U-Pb isotope dilution data reduction and uncertainty propagation: Geochemistry, Geophysics, Geosystems, v. 12, Q0AA19, doi: 10.1029/2010GC003478.

McLean, N.M., Condon, D.J., Condon, B., and Bowring, S.A., 2015, Evaluating uncertainties in the calibration of isotopic reference materials and multi-element isotopic tracers (EARTHTIME tracer calibration II): Geochimica et Cosmochimica, v. 164, p. 481-501, doi: 10.1016/j.gca.2015.02.040.

McNulty, B.A., Tobish, O.T., Cruden, A.R., and Giler, S., 2000, Multistage emplacement of the Mount Givens pluton, central Sierra Nevada batholith, California: Geological Society of America Bulletin, v. 112, p. 119-135, doi: 10.1130/0016-7606(2000)112<119:MEOTMG>2.0.CO;2.

Memeti, V., Paterson, S., Matzel, J., Mundil, R., and Okaya, D., 2010, Magmatic lobes as "snapshots" of magma chamber growth and evolution in large, composite batholiths: An example from the Tuolumne intrusion, Sierra Nevada, California: Geological Society of America Bulletin, v. 122, p. 1912-1931, doi: 10.1130/B30004.1.

Mills, R.D., and Coleman, D.S., 2013, Temporal and chemical connections between plutons and ignimbrites from the Mount Princeton magmatic center: Contributions to Mineralogy and Petrology, v. 165, p. 961-980, doi: 10.1007/s00410-012-0843-4.

Misch, P., 1965, Alkaline granite amidst the calc-alkaline intrusive suite of the Northern Cascades, Washington: Geological Society of America Special Papers, v. 87, p. 216-217.

Rubatto, D., and Hermann, J., 2007, Experimental zircon/melt and zircon/garnet trace element partitioning and implications for the geochronology of crustal rocks: Chemical Geology, v. 241, p. 38-61, doi: 10.1016/j.chemgeo.2007.01.027.

Schmidt, M.W., 1992, Amphibole composition in tonalite as a function of pressure: an experimental calibration of the Al-in-hornblende barometer: Contributions to Mineralogy and Petrology, v. 110, p. 304-310, doi: 10.1007/BF00310745.

Schoene, B., Schaltegger, U., Brack, P., Latkoczy, C., Stracke, A., and Gunther, D., Rates of magma differentiation and emplacement in a ballooning pluton recorded by U-Pb TIMS-TEA, Adamello batholith, Italy: Earth and Planetary Science Letters, v. 355-356, p. 162-173, doi: 10.1016/j.epsl.2012.08.019.

Stelten, M.E., Cooper, K.M., Vazquez, J.A., Calvert, A.T., and Glessner, J.J.G., 2015, Mechanisms and timescales of generating eruptible rhyolitic magmas at Yellowstone caldera from zircon and sanidine geochronology and geochemistry: Journal of Petrology, v. 56, p. 1607-1642, doi: 10.1093/petrology/egv047.

Stull, R.J., 1969, The geochemistry of the southeastern portion of the Golden Horn batholith, Northern Cascades, Washington [Ph.D. thesis]: Seattle, University of Washington, 127 p.

Stull, R.J., 1978, Mantled feldspars from the Golden Horn batholith, Washington: Lithos, v. 11, p. 243-249, doi: 10.1016/0024-4937(78)90024-5.

Tappa, M.J., Coleman, D.S., Mills, R.D., and Samperton, K.M., 2011, The plutonic record of a silicic ignimbrite from the Latir volcanic field, New Mexico: Geochemistry, Geophysics, Geosystems, v. 12, Q10011, doi: 10.1029/2011GC003700.

Figure Captions

Figure DR1: Plot showing the H_2O-saturated eutectic in the quartz (Qz), albite (Ab), orthoclase (Or) system for pressures ranging from 1 to 0.1 GPa (Ebadi and Johannes, 1991). The normative mineralogy for geochemical analyses by Stull (1969) of the peralkaline, hypersolvus, and rapakivi granites are shown and projected using the method of Blundy and Cashman (2001). Compositions for the peralkaline and hypersolvus granites cluster around the 0.2 GPa H_2O-saturated eutectic.

Figure DR2: Back scattered electron (BSE) image of an amphibole in sample NC-MPE-503 from the rapakivi granite of the GHB. The image shows the required assemblage for Al-in-hornblende barometry.

Figure DR3*:* Representative CL images of zircon from granites within the GHB. Oscillatory zoning is clearly seen, indicating an igneous origin. No resorbed cores were seen in any of the images, supporting the inference that GHB magmas intruded above their zircon saturation temperatures.

Figure DR4: Select photomicrographs showing zircon included in major, rock-forming minerals in the granodiorite (NC-MPE-200), hypersolvus granite (NC-MPE-378A), rapakivi granite (NC-MPE-086), and heterogeneous granite (NC-MPE-485). The photomicrograph for NC-MPE-200 is in plane polarized light, while the others are all in cross-polarized light.

Figure DR5: Plot showing the relationship between f_{ThU} and the calculated $[Th/U]_{melt}$ for different $[Th/U]_{zircon}$. The Stelten et al. (2015) value of f_{ThU}=0.138 reproduces the range of whole rock [Th/U] values seen in GHB rocks (Tepper, unpublished data) for the range of $[Th/U]_{zircon}$ seen in our analyses (Table DR4).

Figure DR6: Traditional concordia plots for all of the dated samples presented in this study. All $^{206}Pb/^{238}U$ ratios are Th-corrected. Dates used in weighted mean calculations are shown as red ellipses, those excluded are shown in gray.

Figure DR7: Plot showing volumes and magma emplacement rates for upper crustal granitoid plutons modified from Mills and Coleman (2013) and Frazer et al. (2014). The shaded field represents the rates needed in thermal models to build a large-volume, high-SiO_2 magma chamber (Annen, 2009; Gelman et al., 2013). All emplacement rates represent the mode of Monte Carlo simulations and uncertainties represent the 95% confidence interval. Labels correspond to the numbered intrusive complexes in Table DR6. Volume estimates are limited to the exposed volume (volume = area x topographic relief) to facilitate comparison to the GHB data.

TABLE DR1: ELECTRON MICROPROBE ANALYSES OF HORNBLENDE

Sample Name	SiO_2	TiO_2	K_2O	MnO	Na_2O	Cr_2O_3	Al_2O_3	CaO	FeO_{tot}	MgO	Total*
NC-MPE-503 H1 Core	46.89	1.40	0.64	0.61	1.97	0.01	6.29	10.41	19.80	10.80	98.83
NC-MPE-503 H1 Rim	49.08	0.63	0.47	0.85	1.47	0.00	4.09	10.61	20.68	11.19	99.07
NC-MPE-503 H2 Core	45.75	1.68	0.68	0.52	2.09	0.00	6.85	10.63	21.43	9.26	98.89
NC-MPE-503 H2 Rim	48.68	0.75	0.56	0.83	1.43	0.00	4.75	10.88	20.30	10.59	98.78
NC-MPE-503 H3 Core	44.14	1.59	0.81	0.83	2.23	0.02	7.95	10.59	22.01	9.14	99.32
NC-MPE-503 H3 Rim	46.01	1.58	0.67	0.49	2.18	0.00	6.70	10.45	19.59	10.99	98.65
NC-MPE-503 H4 Core	45.87	1.78	0.67	0.58	2.05	0.00	6.76	10.56	20.74	10.17	99.18
NC-MPE-503 H4 Rim	47.68	0.90	0.63	0.86	1.71	0.00	5.08	10.76	20.75	10.59	98.96
NC-MPE-086 H1 Core	45.87	1.73	0.73	0.68	2.19	0.00	6.82	10.41	20.86	10.16	99.45
NC-MPE-086 H1 Rim	46.21	1.45	0.72	0.64	1.91	0.02	6.77	10.66	20.17	10.46	99.01
NC-MPE-086 H2 Core	47.32	1.10	0.66	0.80	1.86	0.00	5.56	10.62	20.60	10.74	99.26
NC-MPE-086 H2 Rim	46.16	1.35	0.76	0.77	1.88	0.03	6.58	10.59	20.98	9.76	98.86

* All analyses are reported in wt %.

TABLE DR2: ELECTRON MICROPROBE ANALYSES OF PLAGIOCLASE

Sample	SiO_2	CaO	FeO	Na_2O	Al_2O_3	K_2O	Total*
NC-MPE-503 P1 Core	65.91	2.29	0.06	10.50	21.41	0.34	100.52
NC-MPE-503 P1 Rim	67.89	0.59	0.19	11.72	19.85	0.09	100.33
NC-MPE-503 P2 Core	64.44	3.62	0.15	10.01	22.53	0.50	101.25
NC-MPE-503 P2 Rim	65.06	3.06	0.16	9.98	21.89	0.77	100.92
NC-MPE-503 P3 Core	64.19	3.96	0.18	9.32	22.63	0.49	100.77
NC-MPE-503 P3 Rim	66.68	1.76	0.12	10.49	20.89	0.53	100.47
NC-MPE-503 P4 Core	64.80	3.51	0.16	9.88	22.45	0.41	101.22
NC-MPE-503 P4 Rim	68.66	0.97	0.13	11.31	19.88	0.22	101.17
NC-MPE-086 P1 Core	65.72	2.57	0.11	9.98	21.53	0.88	100.79
NC-MPE-086 P1 Rim	66.46	2.06	0.26	10.40	20.89	0.63	100.70
NC-MPE-086 P2 Core	63.87	3.65	0.19	9.10	22.54	0.74	100.08
NC-MPE-086 P2 Rim	66.07	2.40	0.11	10.21	21.25	0.75	100.79

* All measurements are reported in wt %.

TABLE DR3: THERMOBAROMETRY RESULTS

Sample	Al-in-Hornblende Pressure* (GPa)	Plagioclase-Hornblende Temperature† (°C)
NC-MPE-503 H1-P1 Core	0.23	669.4
NC-MPE-503 H1-P1 Rim	0.05	613.5
NC-MPE-503 H2-P2 Core	0.27	686.3
NC-MPE-503 H2-P2 Rim	0.11	630.1
NC-MPE-503 H3-P3 Core	0.30	735.2
NC-MPE-503 H3-P3 Rim	0.26	677.8
NC-MPE-503 H4-P4 Core	0.25	691.6
NC-MPE-503 H4-P4 Rim	0.14	630.5
NC-MPE-086 H1-P1 Core	0.26	690.9
NC-MPE-086 H1-P1 Rim	0.26	676.9
NC-MPE-086 H1-P1 Core	0.17	672.1
NC-MPE-086 H1-P1 Rim	0.25	675.1

* All pressures were calculated using the calibration of Anderson and Smith (1995).
† Temperatures were calculated using Blundy and Holland (1990).

TABLE DR4: CA-ID-TIMS U-Pb ZIRCON GEOCHRONOLOGY RESULTS

Frac.	Dates $^{206}Pb/^{238}U^{*}$	2σ abs.	$^{207}Pb/^{235}U^{\dagger}$	2σ abs.	$^{207}Pb/^{206}Pb^{\dagger}$	2σ abs.	% Disc.[§]	Corr. Coef.	Composition Th/U[#]	Pb_{c} (pg)[*]	Pb*/Pb_{c}[††]	Isotopic Ratios $^{206}Pb/^{204}Pb$[§§]	$^{208}Pb/^{206}Pb$[##]	$^{206}Pb/^{238}U^{*,\#\#}$	2σ %	$^{207}Pb/^{235}U^{\#\#}$	2σ %	$^{207}Pb/^{206}Pb^{*,\#\#}$	2σ %
NC-MPE-438 (48.50682 -120.66447[***])																			
z1	48.467	0.063	48.55	0.42	56	21	14.09	0.275	0.25	0.62	25	1601	0.081	0.0075355	0.086	0.04898	0.88	0.04716	0.86
z2	48.567	0.087	48.96	0.85	72	41	32.64	0.362	0.29	1.98	12	743	0.094	0.007551	0.16	0.04940	1.8	0.04747	1.7
z3	48.472	0.071	48.39	0.62	48	30	-1.38	0.429	0.29	0.48	17	1101	0.092	0.0075361	0.12	0.04881	1.3	0.04699	1.3
z5	48.479	0.092	49.08	0.95	82	46	41.11	0.365	0.32	2.94	10	667	0.104	0.007537	0.18	0.04953	2.0	0.04768	1.9
z6	48.432	0.049	48.41	0.17	51.1	8.1	5.31	0.378	0.31	0.38	69	4374	0.098	0.0075298	0.066	0.04883	0.36	0.04706	0.34
NC-MPE-511 (48.50197 -120.62159[***])																			
z1	48.362	0.033	48.403	0.072	55.1	2.9	12.32	0.625	0.45	0.37	189	11430	0.146	0.0075158	0.067	0.048824	0.15	0.047136	0.12
z3	48.347	0.046	48.57	0.44	64	22	25.11	0.319	0.42	5.20	22	1377	0.135	0.0075134	0.096	0.04900	0.94	0.04732	0.91
z4	48.325	0.033	48.39	0.13	56.1	5.8	13.98	0.456	0.37	0.51	97	5971	0.119	0.0075100	0.067	0.04881	0.27	0.04716	0.24
z5	48.328	0.058	48.35	0.10	54.2	3.9	10.97	0.625	0.40	0.46	193	11798	0.129	0.0075104	0.12	0.04877	0.21	0.047119	0.16
z6	48.357	0.032	48.44	0.13	57.3	6.1	15.73	0.533	0.42	0.41	91	5568	0.136	0.0075151	0.065	0.04886	0.28	0.04718	0.25
z7	48.345	0.034	48.266	0.096	49.0	4.1	1.52	0.570	0.42	0.55	142	8656	0.135	0.0075131	0.071	0.048683	0.20	0.047017	0.17
NC-MPE-093 (48.52964 -120.64862[***])																			
z1	48.247	0.030	48.35	0.19	58.0	9.0	16.98	0.371	0.37	0.75	54	3377	0.118	0.0074978	0.063	0.04877	0.40	0.04719	0.38
z2	48.321	0.073	48.61	0.86	67	42	28.30	0.353	0.41	0.73	12	730	0.132	0.007509	0.15	0.04903	1.8	0.04738	1.8
z6	48.297	0.031	48.36	0.25	56	12	14.11	0.340	0.38	0.35	42	2620	0.123	0.0075056	0.064	0.04878	0.53	0.04716	0.51
z7	48.288	0.054	48.49	0.59	63	29	23.83	0.414	0.39	0.33	18	1099	0.125	0.0075042	0.11	0.04892	1.2	0.04730	1.2
z9	48.24	0.14	48.9	1.7	84	84	42.85	0.329	0.44	1.69	6	368	0.140	0.007496	0.29	0.0493	3.6	0.0477	3.6
z12	48.315	0.050	48.53	0.47	64	23	24.44	0.319	0.39	1.39	21	1300	0.125	0.0075084	0.10	0.04896	1.0	0.04731	0.97
NC-MPE-378A (48.57325 -120.84033[***])																			
z16	48.235	0.062	48.54	0.70	68	34	29.43	0.350	0.38	1.17	14	881	0.123	0.0074960	0.13	0.04897	1.5	0.04740	1.4
z25	48.210	0.038	48.23	0.25	54	12	10.36	0.438	0.39	0.34	46	2830	0.125	0.0074920	0.079	0.04864	0.53	0.04711	0.49
z26	48.228	0.044	48.15	0.35	49	17	1.80	0.247	0.36	0.50	29	1831	0.115	0.0074948	0.091	0.04857	0.74	0.04702	0.72
z27	48.207	0.049	48.18	0.55	51	27	6.50	0.336	0.51	0.69	19	1132	0.162	0.0074915	0.10	0.04859	1.2	0.04707	1.1
z28	48.251	0.055	48.43	0.56	62	27	22.34	0.370	0.94	0.44	23	1241	0.300	0.0074984	0.11	0.04885	1.2	0.04727	1.1
z16	48.235	0.062	48.54	0.70	68	34	29.43	0.350	0.38	1.17	14	881	0.123	0.0074960	0.13	0.04897	1.5	0.04740	1.4
NC-MPE-088 (48.54091 -120.63500[***])																			
z1	48.169	0.065	48.24	0.36	56	17	14.48	0.340	0.40	0.33	30	1840	0.127	0.007486	0.14	0.04865	0.76	0.04716	0.73
z2	48.199	0.042	48.71	0.43	79	21	38.79	0.400	0.38	0.36	24	1523	0.121	0.0074903	0.088	0.04914	0.90	0.04760	0.86
z3	48.205	0.035	48.29	0.30	57	14	15.51	0.393	0.38	0.36	36	2255	0.120	0.0074912	0.072	0.04870	0.63	0.04717	0.60
z4	48.224	0.046	48.50	0.45	67	22	28.12	0.297	0.37	0.23	25	1542	0.120	0.0074942	0.096	0.04893	0.95	0.04737	0.93
z5	48.207	0.053	48.42	0.58	63	28	24.11	0.387	0.37	0.30	18	1109	0.119	0.0074915	0.11	0.04884	1.2	0.04730	1.2
z6	48.223	0.099	48.4	1.3	61	65	21.36	0.289	0.37	0.44	8	496	0.119	0.007494	0.21	0.0488	2.8	0.0473	2.7
NC-MPE-583 (48.55848 -120.69115[***])																			
z1	48.196	0.033	48.39	0.16	62.7	7.2	23.29	0.512	0.38	0.48	78	4818	0.123	0.0074898	0.068	0.04881	0.33	0.04729	0.30
z2	48.164	0.033	48.24	0.21	56	10	14.87	0.379	0.44	0.50	53	3223	0.141	0.0074848	0.067	0.04865	0.45	0.04716	0.43
z3	48.158	0.059	48.43	0.62	66	30	27.67	0.355	0.38	0.74	17	1051	0.121	0.0074838	0.12	0.04885	1.3	0.04736	1.3
z4	48.212	0.057	48.26	0.63	55	31	13.21	0.373	0.41	0.53	16	1005	0.131	0.0074923	0.12	0.04868	1.3	0.04714	1.3
z5	48.256	0.090	48.9	1.1	85	53	43.41	0.343	0.44	1.10	9	583	0.141	0.007499	0.19	0.0493	2.3	0.0477	2.2
z6	48.187	0.030	48.50	0.23	69	11	29.85	0.340	0.39	0.29	47	2931	0.123	0.0074883	0.061	0.04892	0.48	0.04740	0.46
NC-MPE-450 (48.65726 -120.81995[***])																			
z4	48.194	0.074	48.63	0.77	75	37	35.55	0.390	0.37	0.41	14	857	0.118	0.007489	0.15	0.04905	1.6	0.04753	1.6
z5	48.105	0.092	47.8	1.1	36	54	-32.63	0.402	0.39	0.30	10	621	0.126	0.007476	0.19	0.0482	2.3	0.0468	2.2
z6	48.144	0.030	48.30	0.20	60.7	9.8	20.85	0.328	0.35	0.57	51	3195	0.111	0.0074817	0.061	0.04872	0.43	0.04725	0.41
z7	48.119	0.047	48.03	0.51	48	25	0.40	0.390	0.38	0.55	20	1248	0.122	0.0074778	0.098	0.04844	1.1	0.04700	1.1

z8	48.135	0.042	48.43	0.39	68	19	29.17	0.454	0.34	0.42	28	1746	0.108	0.0074803	0.088	0.04886	0.83	0.04739	0.79
z9	48.168	0.039	48.40	0.35	64	17	25.26	0.366	0.36	0.59	29	1806	0.114	0.0074855	0.080	0.04882	0.74	0.04732	0.71
NC-MPE-523 (48.54485 -120.68233***)																			
z2	48.132	0.036	47.99	0.27	46	13	-4.86	0.312	0.34	0.29	44	2724	0.110	0.0074798	0.074	0.04840	0.57	0.04695	0.55
z3	48.129	0.027	48.05	0.14	48.7	6.6	1.28	0.354	0.35	0.34	90	5588	0.113	0.0074794	0.055	0.04846	0.29	0.04701	0.27
z4	48.176	0.035	48.36	0.23	62	11	22.47	0.446	0.34	0.58	48	2981	0.108	0.0074867	0.072	0.04878	0.49	0.04727	0.46
z5	48.185	0.076	48.47	0.74	67	36	28.49	0.416	0.38	1.33	14	906	0.122	0.007488	0.16	0.04889	1.6	0.04738	1.5
z7	48.15	0.10	48.2	1.4	57	71	16.23	0.353	0.33	0.62	8	526	0.105	0.007482	0.21	0.0487	3.1	0.0472	3.0
z8	48.120	0.078	47.65	0.86	29	43	-66.98	0.423	0.39	0.92	13	799	0.124	0.007478	0.16	0.04805	1.8	0.04662	1.8
NC-MPE-086 (48.57338 -120.63071***)																			
z1	48.128	0.029	48.32	0.19	62.6	9.3	23.25	0.230	0.41	0.27	56	3459	0.131	0.0074792	0.059	0.04874	0.40	0.04729	0.39
z2	48.156	0.030	48.23	0.18	56.7	8.9	15.19	0.329	0.56	0.39	63	3706	0.180	0.0074835	0.062	0.04865	0.39	0.04717	0.37
z3	48.098	0.041	48.26	0.29	61	14	21.24	0.363	0.41	0.35	39	2419	0.132	0.0074744	0.085	0.04868	0.62	0.04725	0.60
z4	48.151	0.028	48.28	0.18	59.5	8.6	19.18	0.405	0.40	0.33	67	4091	0.127	0.0074828	0.057	0.04870	0.38	0.04722	0.36
z5	48.134	0.046	48.29	0.17	60.9	7.9	21.08	0.373	0.39	0.41	70	4277	0.126	0.0074801	0.096	0.04871	0.36	0.04725	0.33
z6	48.159	0.058	48.24	0.29	57	15	15.87	0.147	0.74	0.85	39	2197	0.236	0.0074841	0.12	0.04866	0.62	0.04718	0.62
NC-MPE-510 (48.62438 -120.76897***)																			
z1	48.130	0.032	48.15	0.24	54	12	10.77	0.435	0.39	0.34	49	3007	0.126	0.0074795	0.066	0.04856	0.51	0.04711	0.48
z2	48.126	0.045	47.92	0.41	42	20	-13.07	0.343	0.40	0.44	27	1691	0.128	0.0074788	0.094	0.04833	0.87	0.04689	0.84
z3	48.093	0.056	47.84	0.62	40	31	-21.08	0.361	0.33	0.49	16	1021	0.105	0.0074738	0.12	0.04824	1.3	0.04683	1.3
z4	48.152	0.029	48.12	0.21	51	10	6.04	0.273	0.39	0.48	49	3054	0.123	0.0074830	0.059	0.04853	0.44	0.04706	0.42
z5	48.155	0.076	48.58	0.92	74	45	35.42	0.327	0.35	2.63	10	663	0.112	0.007483	0.16	0.04901	1.9	0.04752	1.9
z6	48.109	0.032	48.29	0.26	62	12	22.73	0.404	0.40	0.56	43	2657	0.127	0.0074762	0.067	0.04871	0.54	0.04728	0.52
NC-MPE-499 (48.57868 -120.83591***)																			
z1	48.144	0.080	47.84	0.47	37	23	-28.15	0.310	0.36	0.76	31	1943	0.114	0.007482	0.17	0.04825	1.0	0.04679	0.96
z2	48.148	0.089	48.29	0.22	60	10	19.71	0.431	0.35	0.43	56	3476	0.111	0.007482	0.19	0.04870	0.47	0.04723	0.42
z3	48.119	0.030	48.20	0.19	56.9	9.2	15.64	0.404	0.33	0.51	56	3534	0.106	0.0074778	0.062	0.04862	0.41	0.04717	0.38
z4	48.101	0.033	48.16	0.18	55.5	8.6	13.53	0.349	0.36	0.45	60	3742	0.114	0.0074750	0.069	0.04857	0.38	0.04715	0.36
z5	48.132	0.036	48.19	0.33	56	16	14.17	0.345	0.36	0.44	35	2182	0.115	0.0074798	0.074	0.04861	0.70	0.04715	0.68
z6	48.124	0.045	48.27	0.28	60	14	20.52	0.295	0.39	0.87	38	2347	0.124	0.0074785	0.094	0.04869	0.59	0.04724	0.57
NC-MPE-200 (48.65371 -120.85905***)																			
z1	47.987	0.088	48.3	1.1	67	53	29.02	0.358	0.45	0.58	9	591	0.144	0.007457	0.18	0.0487	2.3	0.0474	2.2
z20	48.004	0.073	47.74	0.87	39	44	-21.89	0.343	0.53	1.14	12	712	0.169	0.007460	0.15	0.04814	1.9	0.04683	1.8
z25	48.080	0.073	48.30	0.87	64	43	25.04	0.342	0.48	1.28	12	716	0.153	0.007472	0.15	0.04872	1.8	0.04731	1.8
z32	48.078	0.059	47.92	0.49	45	24	-7.72	0.512	0.50	0.47	22	1335	0.161	0.0074715	0.12	0.04832	1.1	0.04693	0.99
z33	48.03	0.11	48.8	1.4	90	70	46.82	0.341	0.53	1.84	7	435	0.168	0.007464	0.24	0.0492	3.0	0.0478	2.9
NC-MPE-565A (48.63493 -120.84813***)																			
z1	47.808	0.029	47.83	0.21	53	10	10.57	0.336	0.44	0.31	59	3594	0.140	0.0074292	0.060	0.04823	0.44	0.04710	0.43
z2	47.792	0.046	47.87	0.32	56	16	15.19	0.375	0.54	0.70	34	2047	0.174	0.0074267	0.097	0.04827	0.69	0.04716	0.65
z3	47.732	0.073	47.82	0.43	57	21	16.38	0.375	0.41	0.80	25	1529	0.130	0.007417	0.15	0.04822	0.92	0.04717	0.88
z4	47.820	0.038	47.74	0.38	49	19	1.84	0.332	0.52	0.45	28	1649	0.167	0.0074311	0.080	0.04814	0.81	0.04701	0.79
z5	47.785	0.040	47.75	0.33	50	16	5.50	0.398	0.46	0.25	38	2284	0.146	0.0074255	0.083	0.04815	0.70	0.04705	0.67
NC-MPE-485 (48.66853 -120.90965***)																			
z1	47.73	0.11	47.5	1.3	43	67	-9.99	0.358	0.44	0.54	8	477	0.141	0.007416	0.23	0.0479	2.9	0.0469	2.8
z2	47.743	0.026	47.78	0.11	54.2	5.1	12.11	0.360	0.48	0.39	122	7312	0.155	0.0074191	0.053	0.04818	0.23	0.047119	0.21
z3	47.698	0.059	47.74	0.62	55	31	12.92	0.450	0.44	0.47	16	1000	0.141	0.0074120	0.12	0.04814	1.3	0.04713	1.3
z4	47.725	0.029	47.71	0.14	51.8	6.5	8.07	0.655	0.40	0.21	109	6721	0.127	0.0074162	0.061	0.04811	0.31	0.04707	0.27
z5	47.723	0.028	47.69	0.18	50.7	8.6	6.11	0.354	0.39	0.25	66	4096	0.124	0.0074159	0.058	0.04809	0.38	0.04705	0.36
z6	47.952	0.045	48.04	0.48	57	23	16.07	0.409	0.44	0.35	22	1361	0.140	0.0074517	0.094	0.04845	1.0	0.04718	0.98
NC-MPE-517 (48.63261 -120.80870***)																			

z1	48.344	0.044	48.58	0.46	65	23	25.56	0.340	0.39	1.03	21	1322	0.126	0.0075129	0.092	0.04901	0.98	0.04733	0.95
z2	48.603	0.062	48.33	0.65	39	32	-23.59	0.404	0.25	0.32	15	993	0.079	0.0075533	0.13	0.04874	1.4	0.04683	1.3
z4	48.266	0.054	48.40	0.48	60	23	19.05	0.384	0.44	0.40	24	1498	0.141	0.0075008	0.11	0.04882	1.0	0.04722	0.97
z5	47.988	0.052	48.30	0.49	68	24	30.00	0.380	0.79	0.66	25	1411	0.252	0.0074573	0.11	0.04872	1.0	0.04740	1.0
z6	48.198	0.033	48.33	0.27	59	13	19.04	0.360	0.42	0.47	39	2421	0.133	0.0074901	0.069	0.04875	0.57	0.04722	0.55
z7	48.13	0.19	48.5	2.4	73	120	34.31	0.364	0.93	0.69	5	274	0.297	0.007480	0.39	0.0490	5.1	0.0475	4.9
z8	48.192	0.030	48.07	0.13	46.8	5.9	-2.73	0.447	0.51	0.47	117	6941	0.164	0.0074891	0.062	0.04848	0.27	0.04697	0.24

* Corrected for initial Th/U disequilibrium using radiogenic ^{208}Pb and f_{ThU}=0.138 for granitoids (Stelten et al., 2015) or f_{ThU}=0.33 for the diorite (Rubatto and Hermann, 2007).
† Isotopic dates calculated using the decay constants λ238 = 1.55125E-10 and λ235 = 9.8485E-10 (Jaffey et al. 1971).
§ % discordance = 100 - (100 * ($^{206}Pb/^{238}U$ date) / ($^{207}Pb/^{206}Pb$ date))
# Th contents calculated from radiogenic ^{208}Pb and the $^{207}Pb/^{206}Pb$ date of the sample, assuming concordance between U-Th and Pb systems.
** Total mass of common Pb.
†† Ratio of radiogenic Pb (including ^{208}Pb) to common Pb.
§§ Measured ratio corrected for fractionation and spike contribution only.
Measured ratios corrected for fractionation, tracer and blank.
*** All locations reported using WGS 84.

TABLE DR5: COMPARISON OF DIFFERENT Th-CORRECTION METHODS

Sample	Weighted Mean $^{206}Pb/^{238}U$ Date (Ma) Constant f_{ThU}* Correction	Weighted Mean $^{206}Pb/^{238}U$ Date (Ma) Constant $[Th/U]_{Magma}$† Correction	Difference Between Methods (Ma)
NC-MPE-438	48.468 ± 0.030/0.037/0.064 (MSWD=1.84)	48.485 ± 0.022/0.031/0.060 (MSWD=2.87)	0.017
NC-MPE-511	48.346 ± 0.015/0.026/0.058 (MSWD=0.69)	48.345 ± 0.015/0.026/0.058 (MSWD=0.60)	0.001
NC-MPE-093	48.281 ± 0.018/0.028/0.059 (MSWD=1.91)	48.281 ± 0.018/0.028/0.059 (MSWD=1.88)	0.000
NC-MPE-378A	48.223 ± 0.021/0.030/0.060 (MSWD=0.54)	48.219 ± 0.021/0.030/0.060 (MSWD=0.34)	0.004
NC-MPE-088	48.205 ± 0.020/0.030/0.060 (MSWD=0.42)	48.205 ± 0.020/0.030/0.060 (MSWD=0.44)	0.000
NC-MPE-583	48.185 ± 0.016/0.027/0.058 (MSWD=1.27)	48.185 ± 0.016/0.027/0.058 (MSWD=1.29)	0.000
NC-MPE-450	48.146 ± 0.018/0.028/0.059 (MSWD=1.08)	48.147 ± 0.018/0.028/0.059 (MSWD=1.09)	0.001
NC-MPE-523	48.144 ± 0.017/0.027/0.058 (MSWD=1.33)	48.146 ± 0.017/0.027/0.058 (MSWD=1.35)	0.002
NC-MPE-086	48.139 ± 0.014/0.025/0.057 (MSWD=1.44)	48.136 ± 0.014/0.026/0.057 (MSWD=1.19)	0.003
NC-MPE-510	48.129 ± 0.016/0.026/0.058 (MSWD=1.26)	48.129 ± 0.016/0.026/0.058 (MSWD=1.24)	0.000
NC-MPE-499	48.120 ± 0.017/0.027/0.058 (MSWD=0.50)	48.121 ± 0.017/0.027/0.058 (MSWD=0.50)	0.001
NC-MPE-200	48.045 ± 0.034/0.041/0.066 (MSWD=1.33)	48.041 ± 0.034/0.041/0.066 (MSWD=1.32)	0.004
NC-MPE-565A	47.799 ± 0.018/0.028/0.058 (MSWD=1.38)	47.796 ± 0.018/0.028/0.058 (MSWD=1.30)	0.003
NC-MPE-485	47.729 ± 0.015/0.026/0.057 (MSWD=0.64)	47.727 ± 0.015/0.026/0.057 (MSWD=0.53)	0.002
NC-MPE-517	47.988 ± 0.052/0.056/0.076 (Max. Age)	47.972 ± 0.053/0.057/0.077 (Max. Age)	0.016

*f_{ThU}=0.138 for granitoids (Stelten et al., 2015) or f_{ThU}=0.33 for the diorite (Rubatto and Hermann, 2007).
†$[Th/U]_{Magma}$= 2.8 ± 1.0 (2σ) for all samples.

TABLE DR6: MAGMA EMPLACEMENT RATES IN UPPER CRUSTAL GRANITOID PLUTONS

Intrusive Complex	Intrusion Depth (km)	Area (km^2)	Vertical Relief (km)	Volume (km^3)	Oldest Date (Ma)*	Youngest Date (Ma)*	Emplacement Rate (km^3/yr) †	References
1) Lago della Vacca pluton	12	9.7	1.0	10	42.07 ± 0.04	41.76 ± 0.03	0.00003	John and Blundy (1993), Schoene et al. (2012)
2) Lamarck granodiorite	8-12	600	3.0	1800	94.26 ± 0.17	90.9 ± 0.2	0.00053	Davis et al. (2012)
3) Mt. Givens granodiorite	9	1500	3.0	4500	97.92 ± 0.06	90.87 ± 0.05	0.00133	McNulty et al. (2002), Frazer et al. (2014)
4) Mt. Princeton batholith	3	450	1.5	675	35.80 ± 0.09	35.37 ± 0.10	0.00153	Mills and Coleman (2013)
5) Mt. Stuart batholith (Old Domain)	6-12	194	2.5	485	95.88 ± 0.03	94.25 ± 0.14	0.00030	Matzel et al. (2006)
6) Mt. Stuart batholith (Young Domain)	6-12	208	2.5	520	90.92 ± 0.05	90.78 ± 0.08	0.00316	Matzel et al. (2006)
7) Muir intrusive suite	8-12	1700	3.0	5100	95.45 ± 0.32	83.5 ± 0.5§	0.00043	Davis et al. (2012)
8) Rio Honda pluton	< 5	90	1.2	108	22.98 ± 0.09	22.59 ± 0.06	0.00027	Tappa et al. (2011)
9) Torres del Paine complex	2-3	80	2.0	88	12.593 ± 0.009	12.431 ± 0.006	0.00054	Leuthold et al. (2012)
10) Tuolumne intrusive suite	3-9	1200	2.0	2400	94.4 ± 0.3	85.1 ± 0.9	0.00026	Coleman et al. (2004), Memeti et al. (2010)

* ID-TIMS $^{206}Pb/^{238}U$ zircon dates

† Emplacement rates were calculated using the mode of Monte Carlo simulations with 10^7 iterations

§ The uncertainty for this sample was not reported in Davis et al. (2011), we apply a conservative estimate of 0.5 Ma

Figure DR1

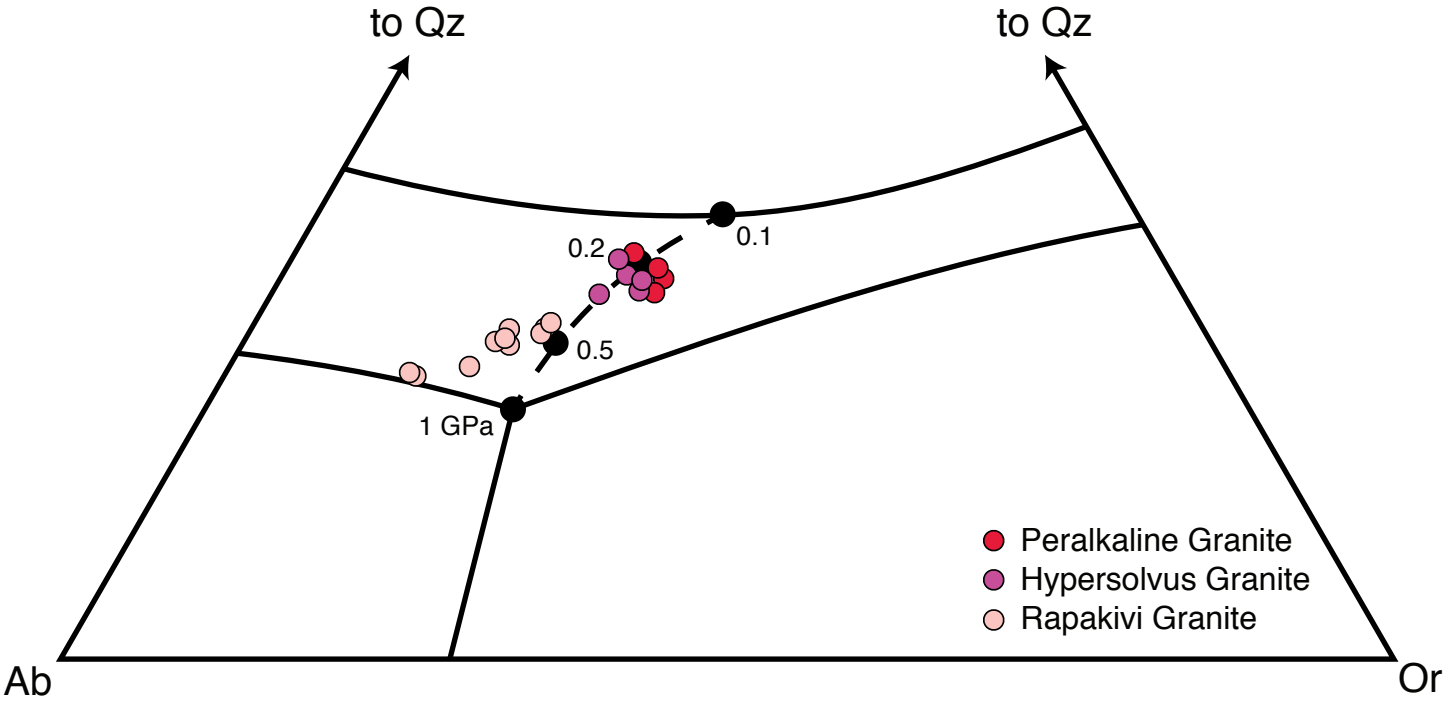

Figure DR2

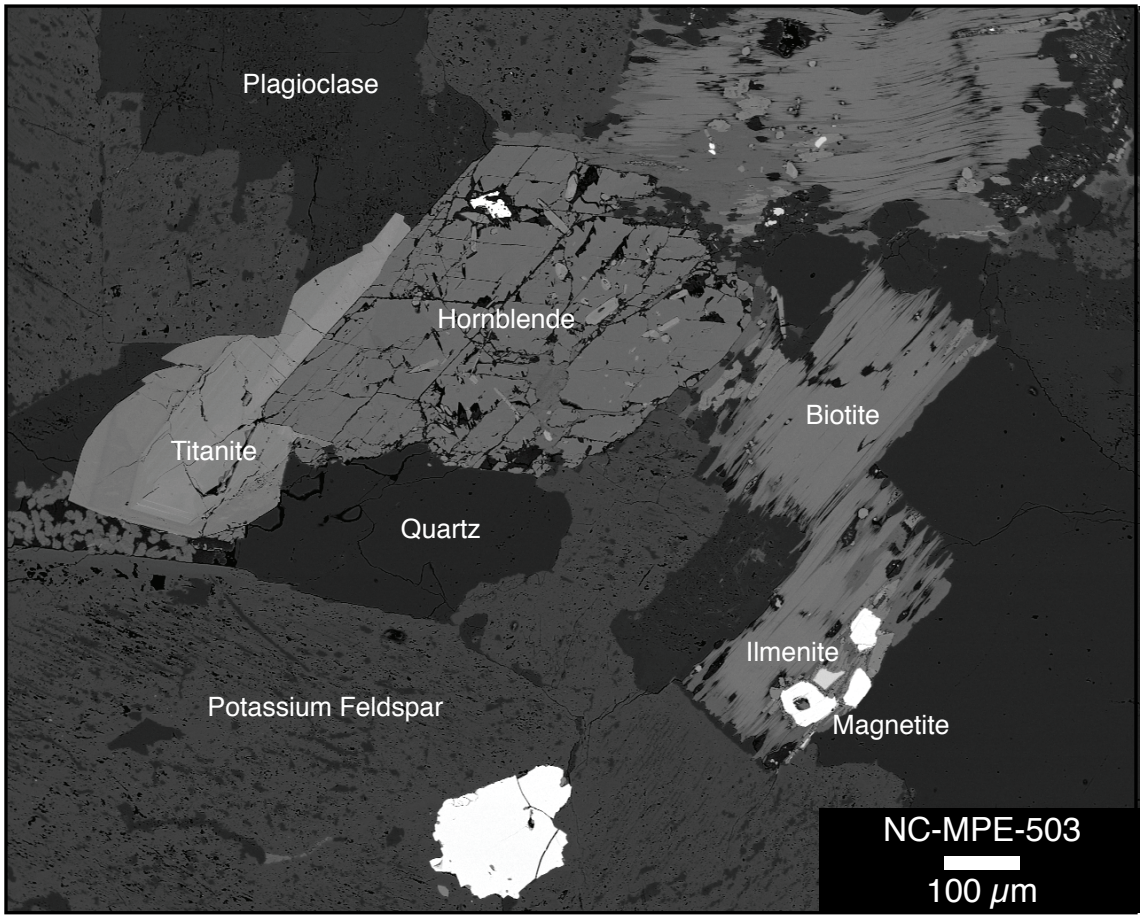

Figure DR3

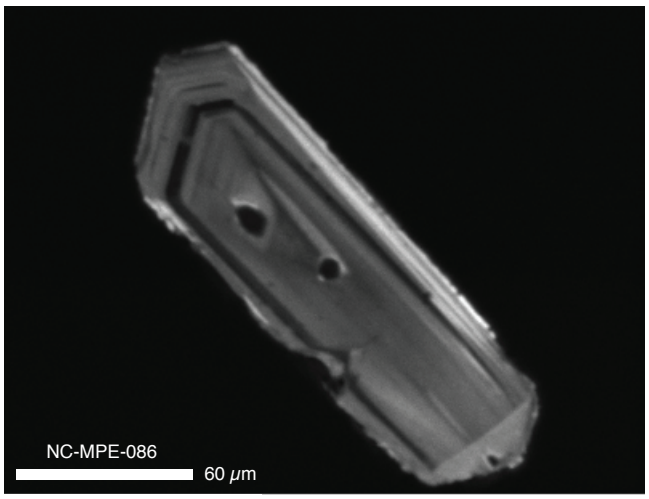

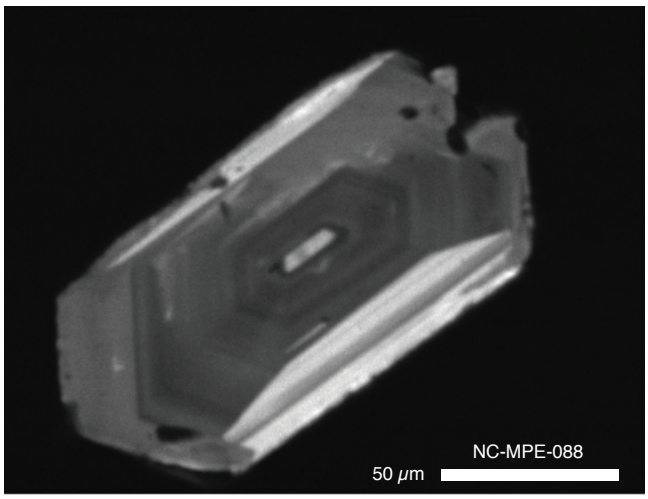

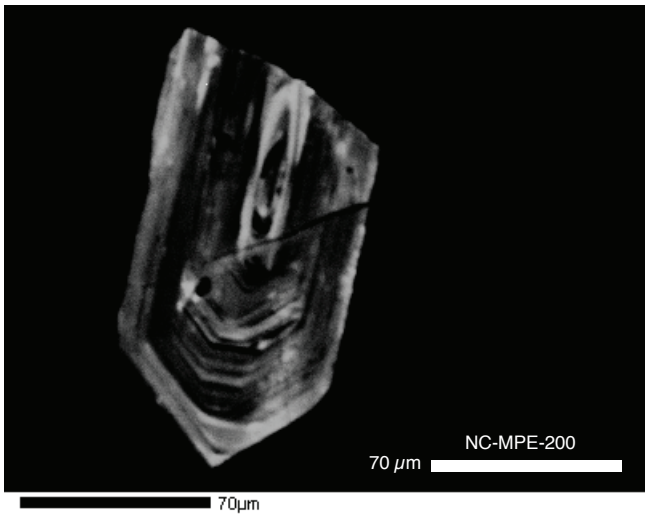

CL NC-MPE-200 z19

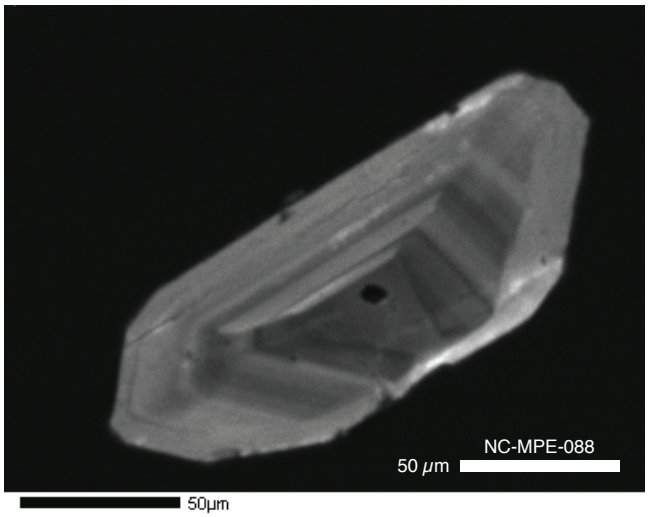

CL NC-MPE-088 z17

Figure DR4

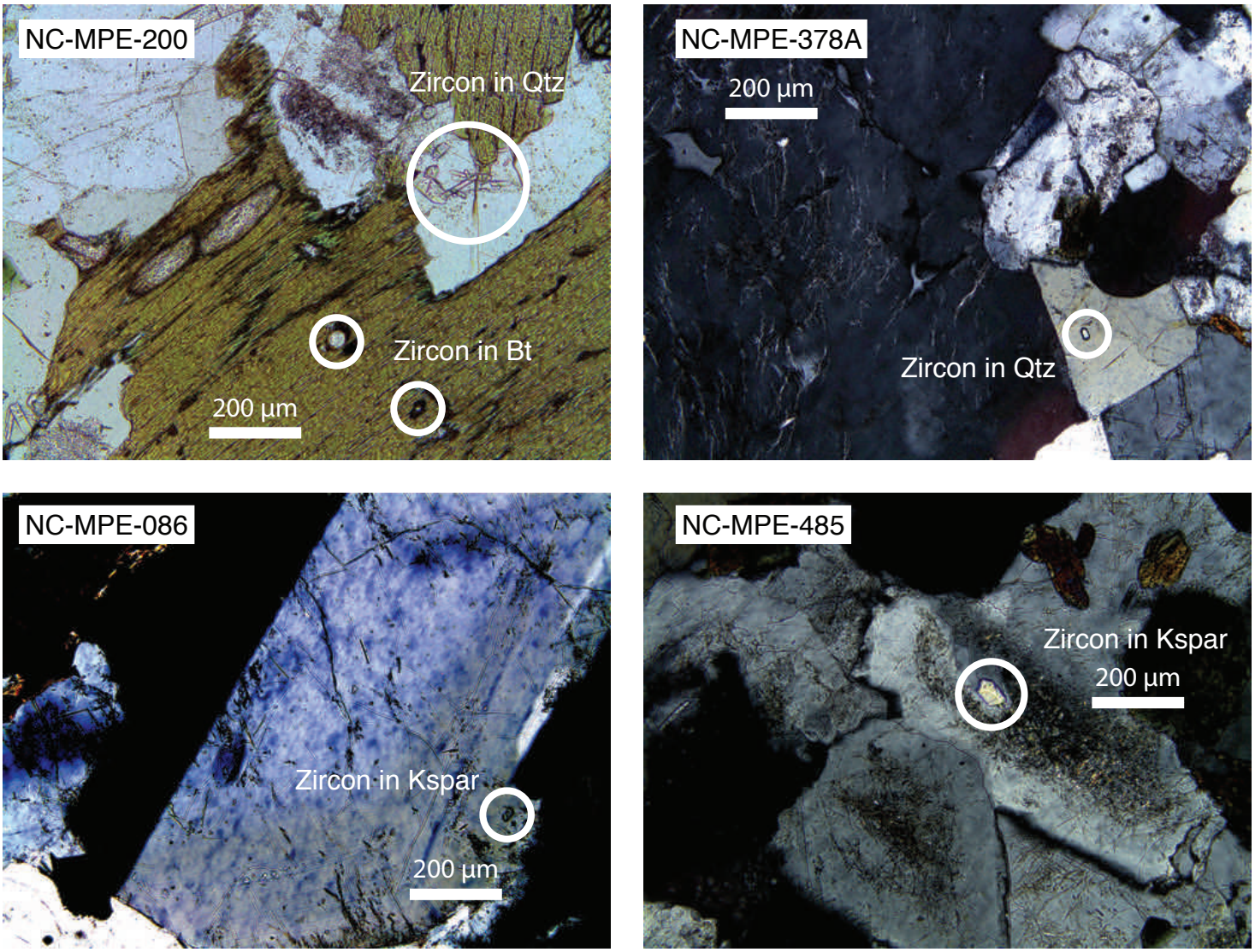

Figure DR5

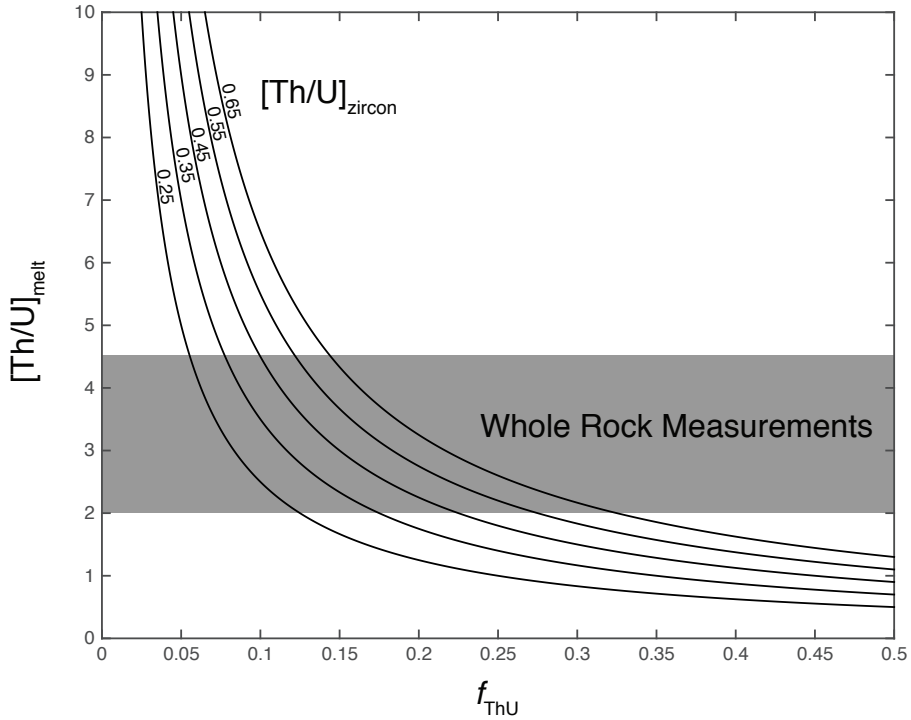

Figure DR6

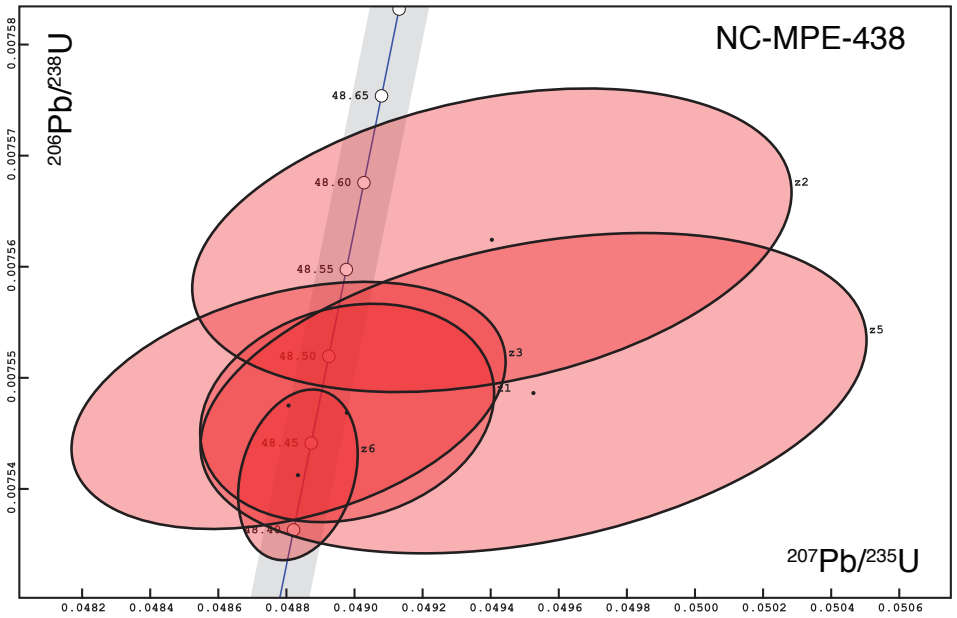
NC-MPE-438
206Pb/238U
207Pb/235U
48.65
48.60
48.55
48.50
48.45
48.40
z1
z2
z3
z5
z6
0.00758
0.00757
0.00756
0.00755
0.00754
0.0482
0.0484
0.0486
0.0488
0.0490
0.0492
0.0494
0.0496
0.0498
0.0500
0.0502
0.0504
0.0506

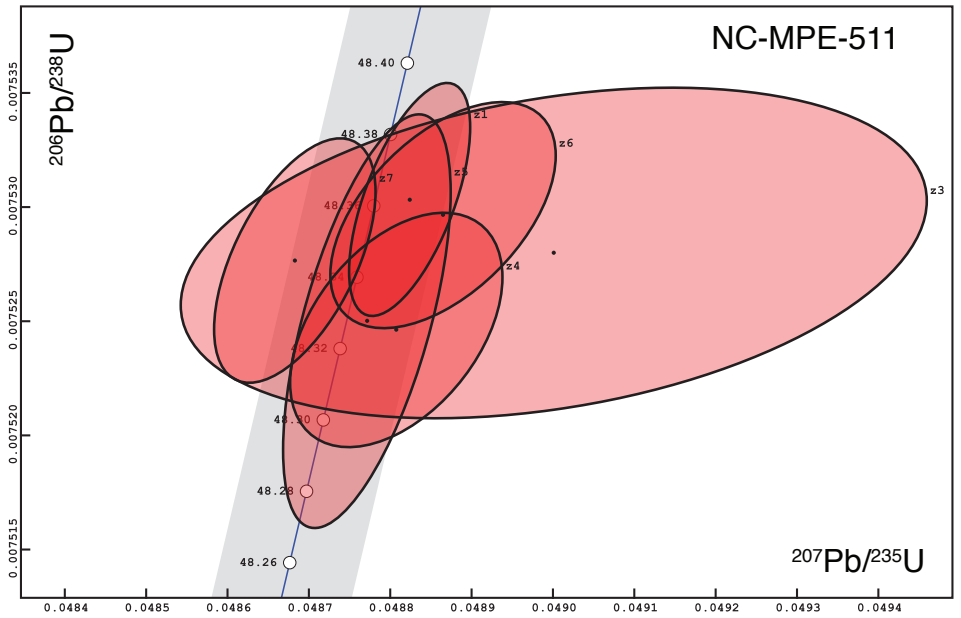
NC-MPE-511
206Pb/238U
207Pb/235U
48.40
48.38
48.30
48.28
48.26
z1
z3
z4
z6
z7
0.007535
0.007530
0.007525
0.007520
0.007515
0.0484
0.0485
0.0486
0.0487
0.0488
0.0489
0.0490
0.0491
0.0492
0.0493
0.0494

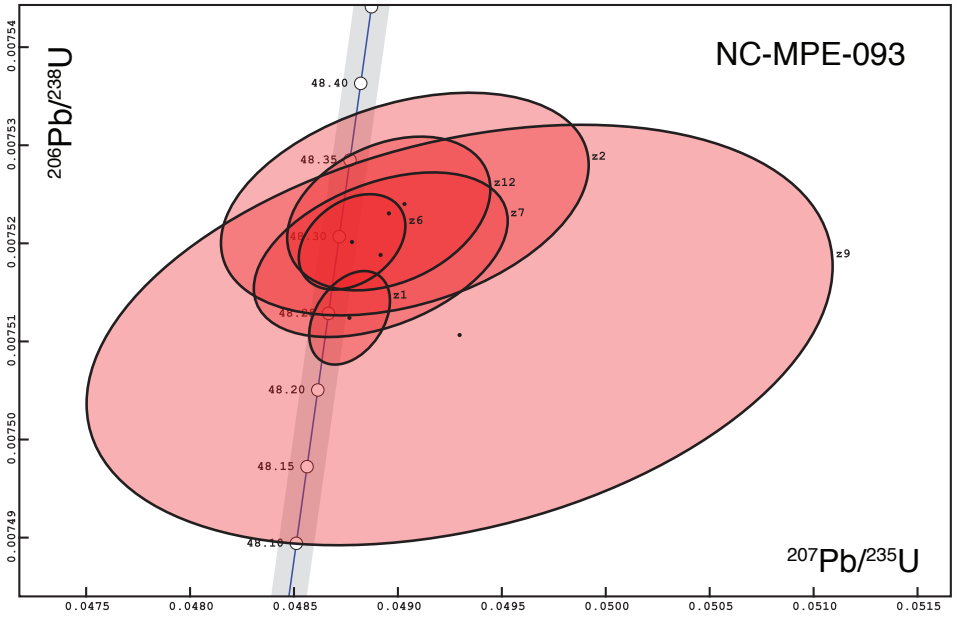
NC-MPE-093
206Pb/238U
207Pb/235U
48.40
48.35
48.30
48.25
48.20
48.15
48.10
z1
z2
z6
z7
z9
z12
0.00754
0.00753
0.00752
0.00751
0.00750
0.00749
0.0475
0.0480
0.0485
0.0490
0.0495
0.0500
0.0505
0.0510
0.0515

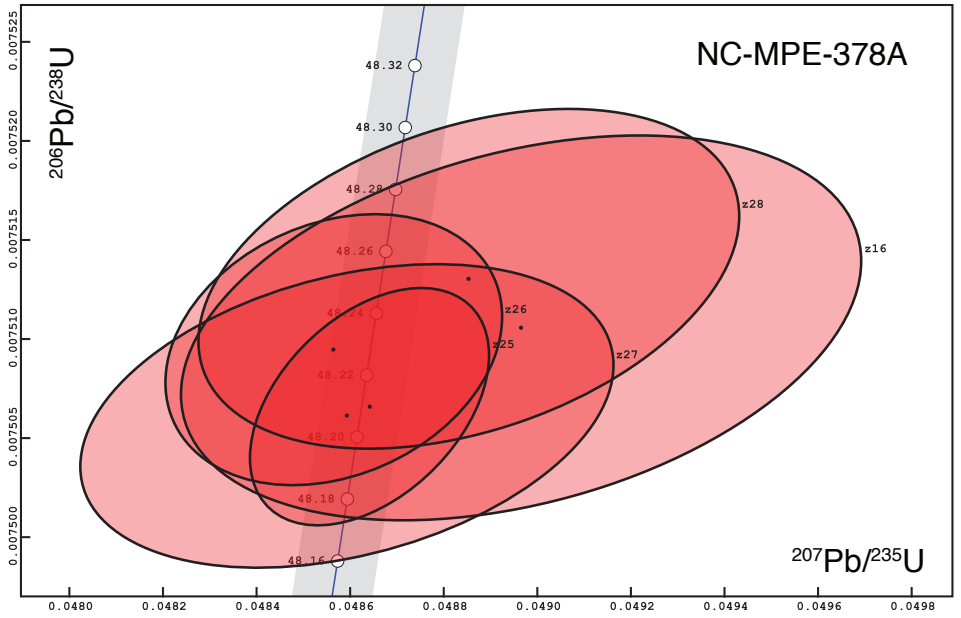
NC-MPE-378A
206Pb/238U
207Pb/235U
48.32
48.30
48.28
48.26
48.24
48.22
48.20
48.18
48.16
z16
z25
z26
z27
z28
0.007525
0.007520
0.007515
0.007510
0.007505
0.007500
0.0480
0.0482
0.0484
0.0486
0.0488
0.0490
0.0492
0.0494
0.0496
0.0498

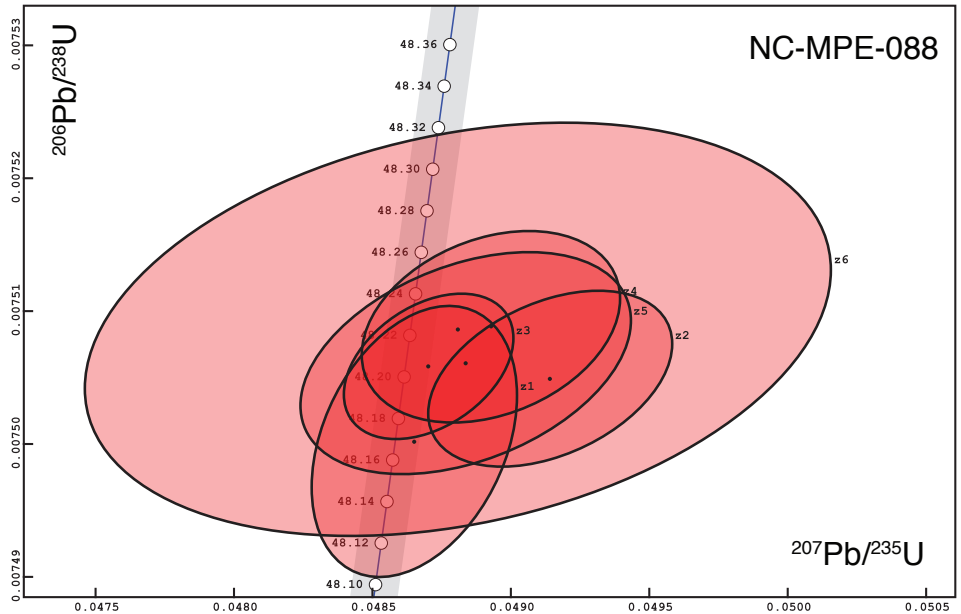
NC-MPE-088
$^{206}Pb/^{238}U$
$^{207}Pb/^{235}U$
48.36
48.34
48.32
48.30
48.28
48.26
48.24
48.22
48.20
48.18
48.16
48.14
48.12
48.10
z1
z2
z3
z4
z5
z6
0.00753
0.00752
0.00751
0.00750
0.00749
0.0475
0.0480
0.0485
0.0490
0.0495
0.0500
0.0505

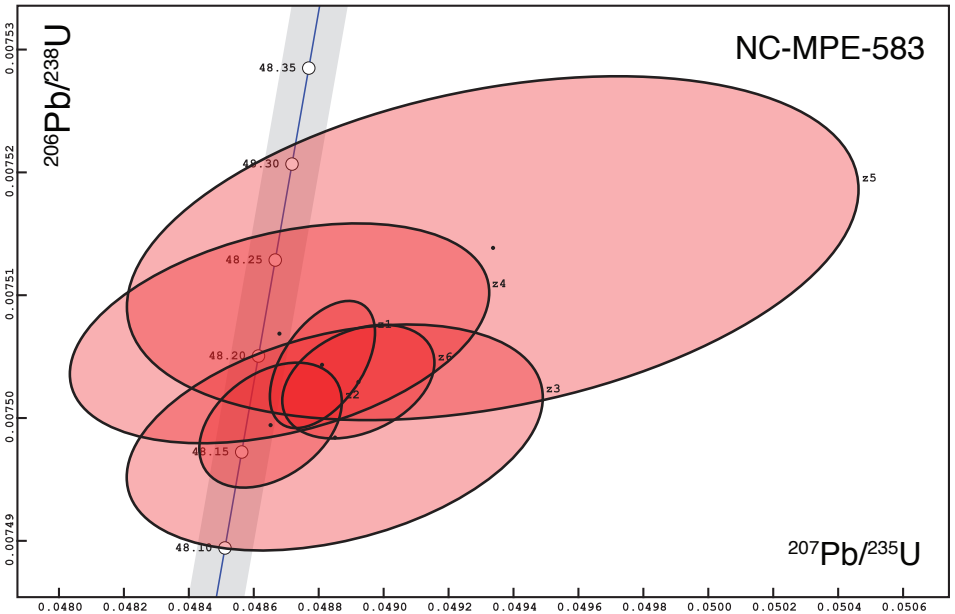
NC-MPE-583
$^{206}Pb/^{238}U$
$^{207}Pb/^{235}U$
48.35
48.30
48.25
48.20
48.15
48.10
z1
z2
z3
z4
z5
z6
0.00753
0.00752
0.00751
0.00750
0.00749
0.0480
0.0482
0.0484
0.0486
0.0488
0.0490
0.0492
0.0494
0.0496
0.0498
0.0500
0.0502
0.0504
0.0506

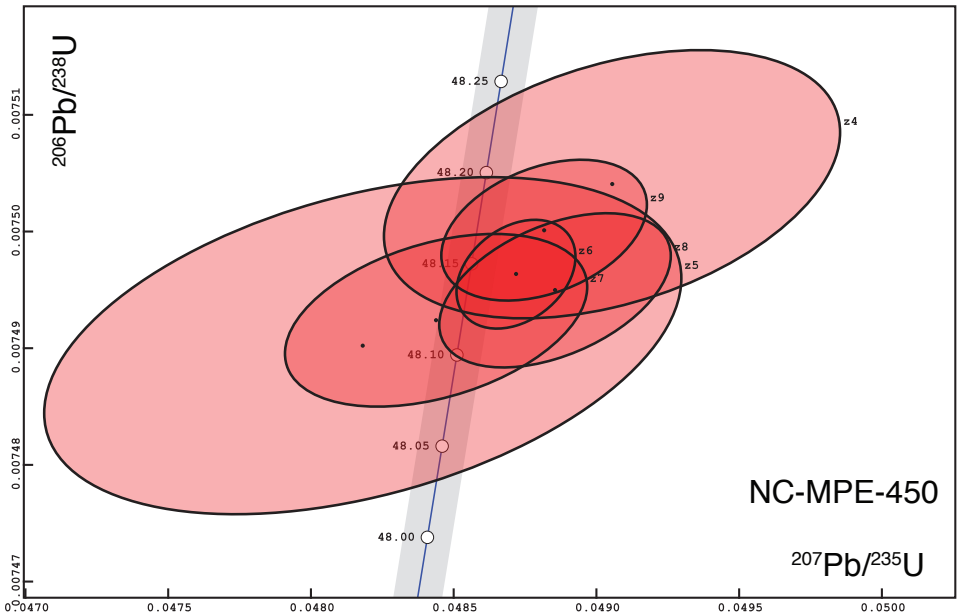
NC-MPE-450
$^{206}Pb/^{238}U$
$^{207}Pb/^{235}U$
48.25
48.20
48.15
48.10
48.05
48.00
z4
z5
z6
z7
z8
z9
0.00751
0.00750
0.00749
0.00748
0.00747
0.0470
0.0475
0.0480
0.0485
0.0490
0.0495
0.0500

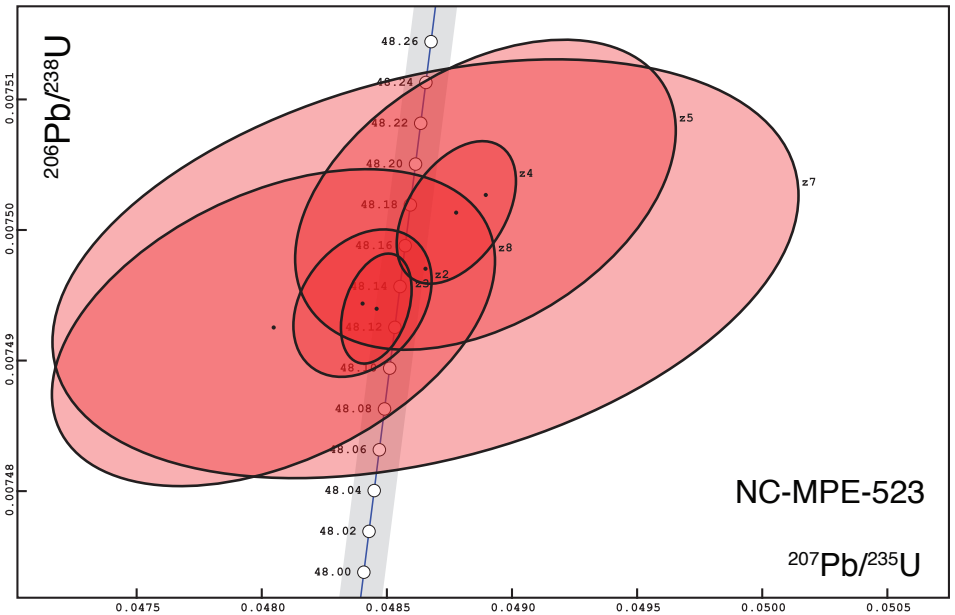
NC-MPE-523
$^{206}Pb/^{238}U$
$^{207}Pb/^{235}U$
48.26
48.24
48.22
48.20
48.18
48.16
48.14
48.12
48.10
48.08
48.06
48.04
48.02
48.00
z2
z3
z4
z5
z7
z8
0.00751
0.00750
0.00749
0.00748
0.0475
0.0480
0.0485
0.0490
0.0495
0.0500
0.0505

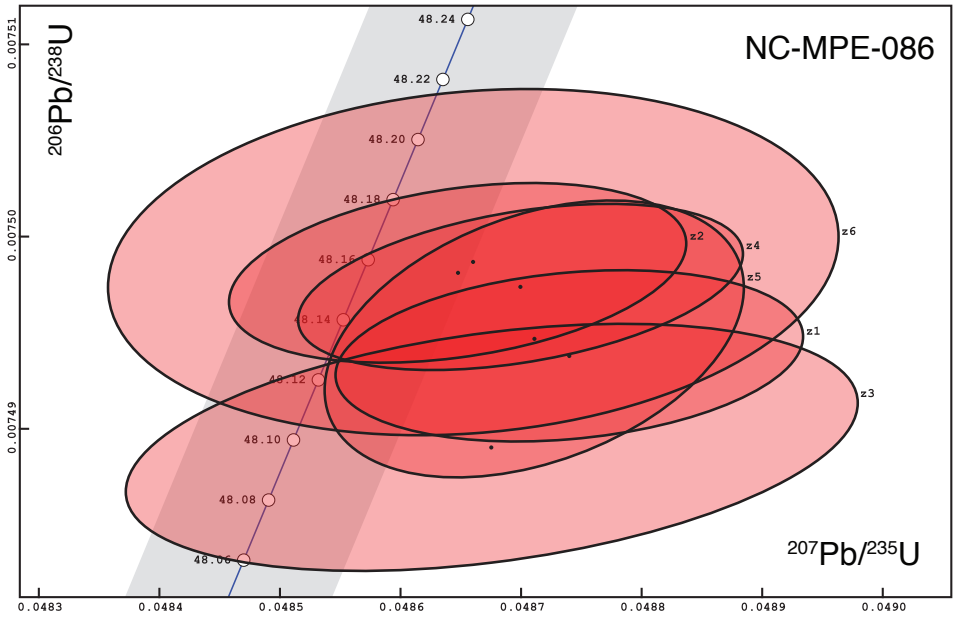
NC-MPE-086
206Pb/238U
207Pb/235U
48.24
48.22
48.20
48.18
48.16
48.14
48.12
48.10
48.08
48.06
z1
z2
z3
z4
z5
z6
0.00751
0.00750
0.00749
0.0483
0.0484
0.0485
0.0486
0.0487
0.0488
0.0489
0.0490

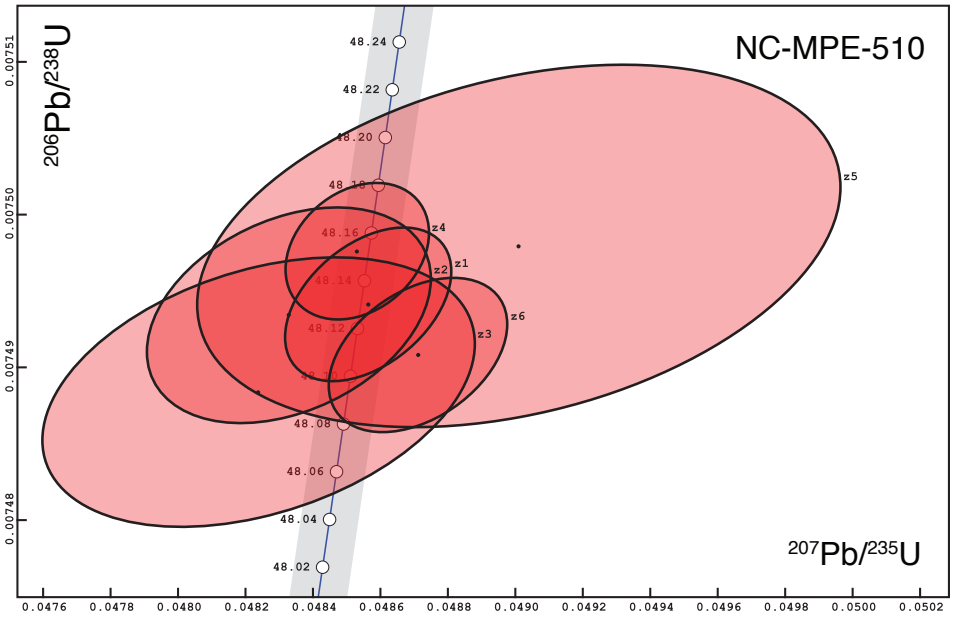
NC-MPE-510
206Pb/238U
207Pb/235U
48.24
48.22
48.20
48.18
48.16
48.14
48.12
48.08
48.06
48.04
48.02
z1
z2
z3
z4
z5
z6
0.00751
0.00750
0.00749
0.00748
0.0476
0.0478
0.0480
0.0482
0.0484
0.0486
0.0488
0.0490
0.0492
0.0494
0.0496
0.0498
0.0500
0.0502

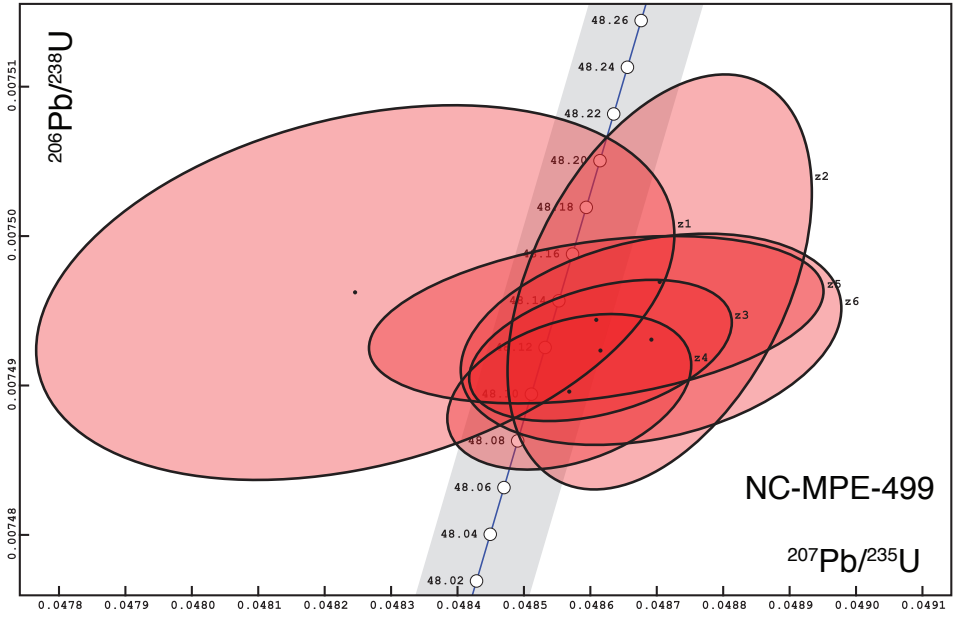
NC-MPE-499
206Pb/238U
207Pb/235U
48.26
48.24
48.22
48.20
48.18
48.16
48.08
48.06
48.04
48.02
z1
z2
z3
z4
z6
z6
0.00751
0.00750
0.00749
0.00748
0.0478
0.0479
0.0480
0.0481
0.0482
0.0483
0.0484
0.0485
0.0486
0.0487
0.0488
0.0489
0.0490
0.0491

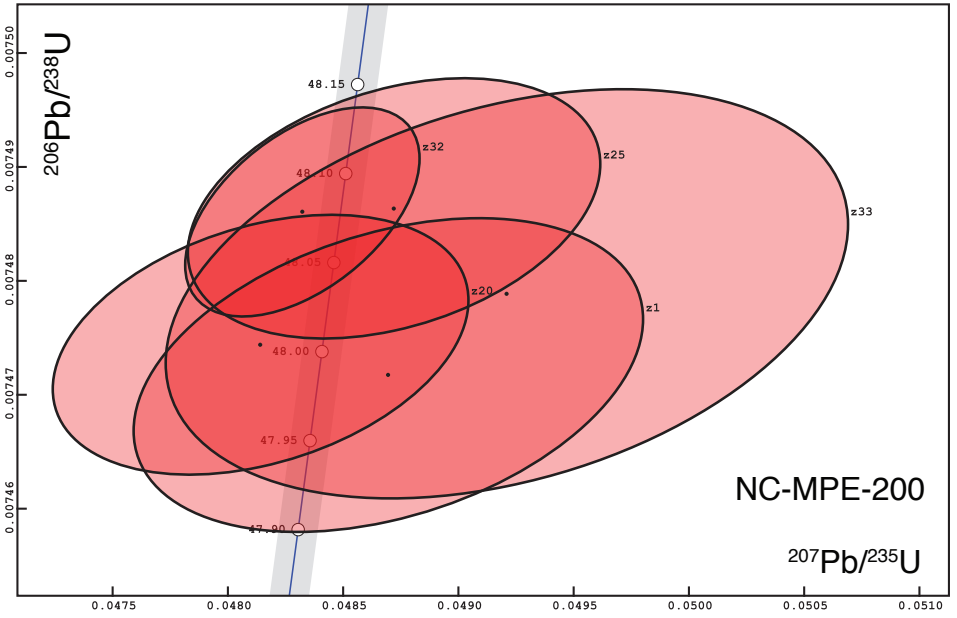
NC-MPE-200
206Pb/238U
207Pb/235U
48.15
48.10
48.00
47.95
47.90
z1
z20
z25
z32
z33
0.00750
0.00749
0.00748
0.00747
0.00746
0.0475
0.0480
0.0485
0.0490
0.0495
0.0500
0.0505
0.0510

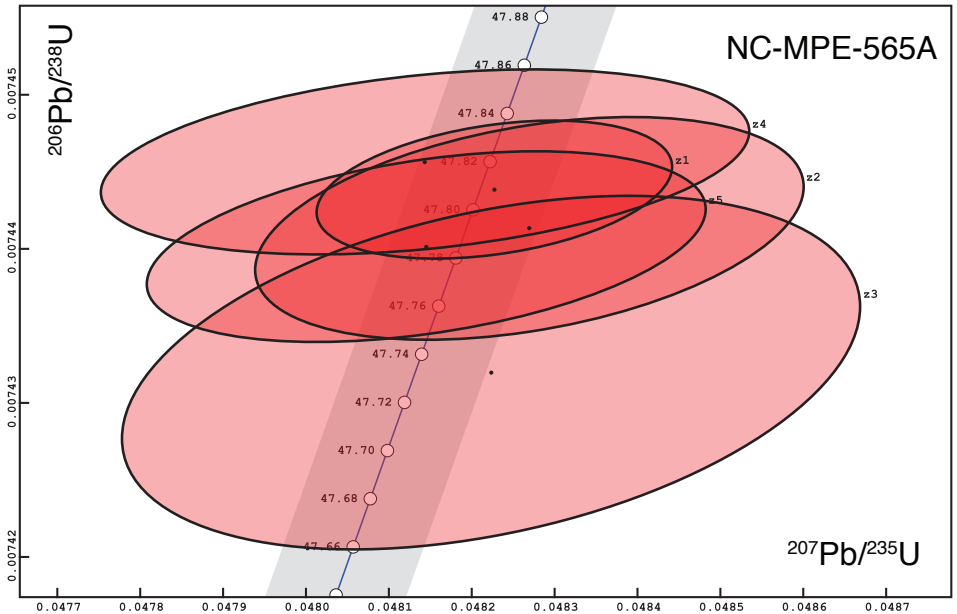
NC-MPE-565A
206Pb/238U
207Pb/235U
47.88
47.86
47.84
47.82
47.80
47.78
47.76
47.74
47.72
47.70
47.68
47.66
z1
z2
z3
z4
z5
0.00745
0.00744
0.00743
0.00742
0.0477
0.0478
0.0479
0.0480
0.0481
0.0482
0.0483
0.0484
0.0485
0.0486
0.0487

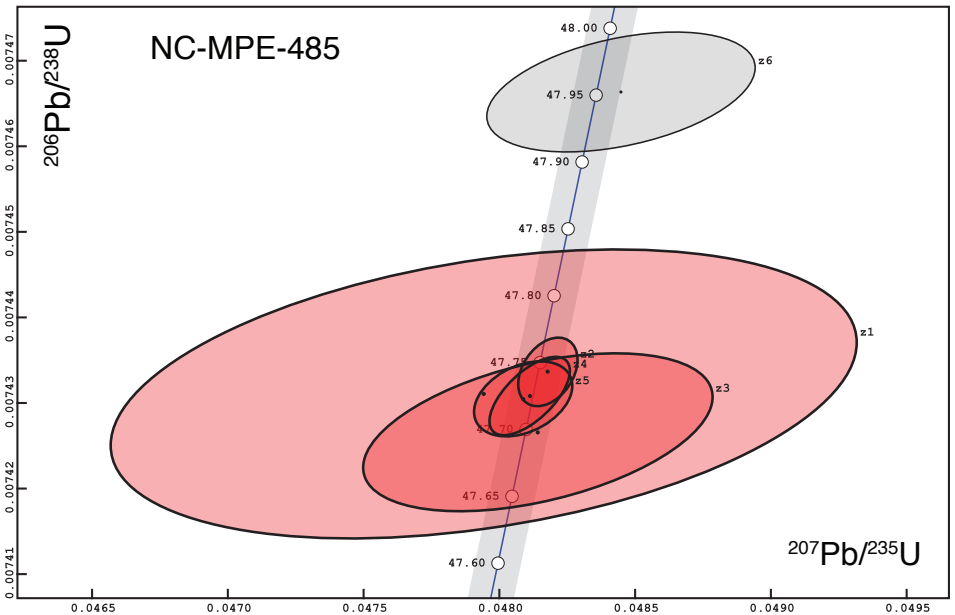
NC-MPE-485
206Pb/238U
207Pb/235U
48.00
47.95
47.90
47.85
47.80
47.75
47.70
47.65
47.60
z1
z2
z3
z4
z5
z6
0.00747
0.00746
0.00745
0.00744
0.00743
0.00742
0.00741
0.0465
0.0470
0.0475
0.0480
0.0485
0.0490
0.0495

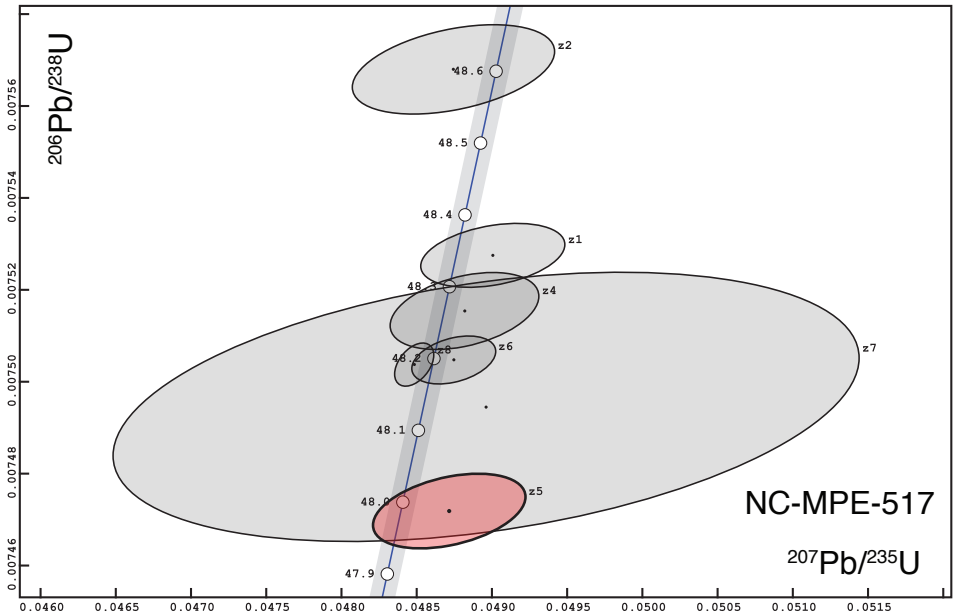
NC-MPE-517
206Pb/238U
207Pb/235U
48.6
48.5
48.4
48.3
48.2
48.1
48.0
47.9
z1
z2
z4
z5
z6
z7
0.00756
0.00754
0.00752
0.00750
0.00748
0.00746
0.0460
0.0465
0.0470
0.0475
0.0480
0.0485
0.0490
0.0495
0.0500
0.0505
0.0510
0.0515

Figure DR7

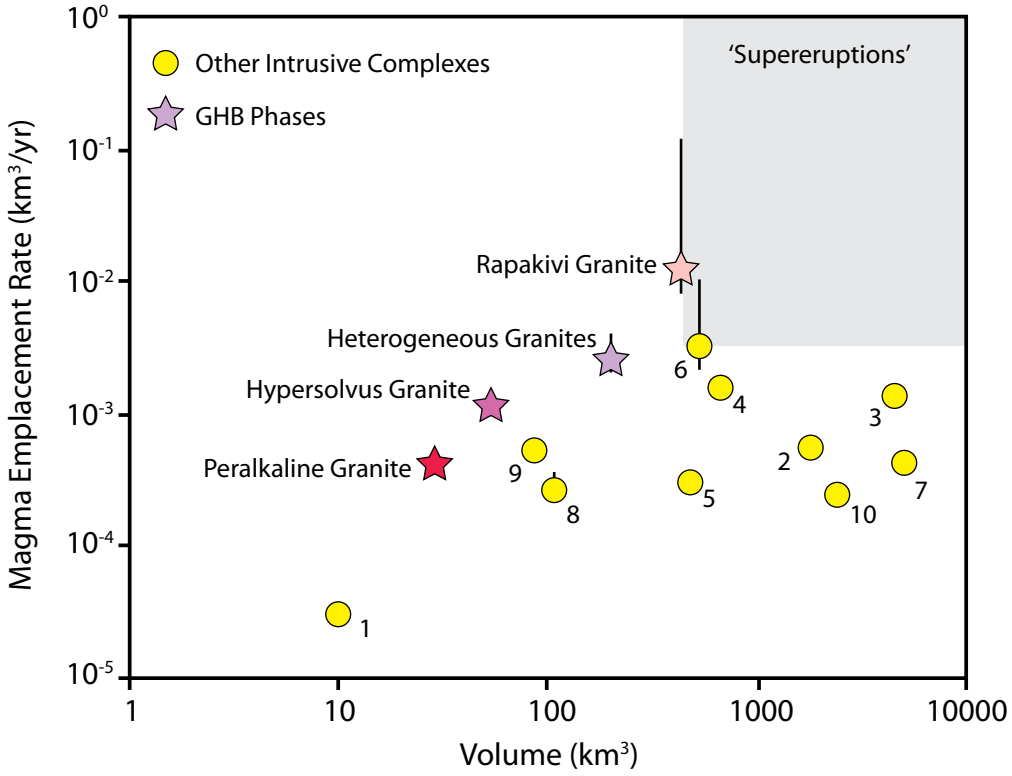
Other Intrusive Complexes
GHB Phases
'Supereruptions'
Rapakivi Granite
Heterogeneous Granites
Hypersolvus Granite
Peralkaline Granite
1
2
3
4
5
6
7
8
9
10
Magma Emplacement Rate (km³/yr)
Volume (km³)
10⁰
10⁻¹
10⁻²
10⁻³
10⁻⁴
10⁻⁵
1
10
100
1000
10000